



Passive satellite hourly precipitation estimation over mainland China by combining cloud and meteorological parameters

Sihang Xu^a, Jiming Li^{a,b,*}, Jia Li^a, Deyu Wen^a, Miao Lei^a, Yuan Wang^b, Jianping Huang^{a,b}

^a College of Atmospheric Sciences, Lanzhou University, Lanzhou 730000, China

^b Collaborative Innovation Center for Western Ecological Safety, Lanzhou University, Lanzhou 730000, China

ARTICLE INFO

Keywords:

Hourly precipitation estimation
Cloud property
Passive satellite
Effective variables
Meteorological factor

ABSTRACT

High-quality satellite quantitative precipitation estimation (QPE) is crucial for theoretical studies and disaster monitoring. However, it remains unclear which information is effective or relatively less valuable. Accurately eliminating ineffective variables and applying effective ones as predictors can further enhance the accuracy and computational efficiency for QPE. In this study, an hourly QPE algorithm was developed using three machine learning (ML) models, including Random Forest, XGBoost and LightGBM. We focused on obtaining high-precision precipitation estimations and further analyzing the contribution of different input variables. Sensitivity experiments revealed that satellite visible channels and cloud properties are key factors for accurate QPE. In contrast, information provided solely by infrared channels and meteorological variables is relatively limited. Among three ML models, LightGBM achieved the best QPE, and was comparable to, or even slightly better than GPM IMERG, which may be attributed to its incorporation of more effective variables and training with ground rain gauge. However, it sometimes underestimates heavy precipitation compared to GPM IMERG, probably due to few training samples and saturation of satellite spectral signals. The analysis of Shapley Additive Explanations (SHAP) indicates that QPE are more sensitive to cloud properties (e.g., cloud water path), but some meteorological factors, such as relative humidity at different pressure levels are becoming more important as the environment becomes drier. Additionally, the performance of ML model and GPM IMERG deeply relies on cloud type. These findings are expected to provide valuable references for the construction of future satellite QPE algorithms in terms of feature selection and data processing.

1. Introduction

As a commonly weather phenomena, precipitation is a key driving variable of the global hydrological cycle and is also a significant element of the Earth-atmospheric system energy budget, water resource management and ecological studies (Chen and Pfaendtner, 1993; Stephens et al., 2012; Duncan et al., 2013; Nielsen and Ball, 2015). On one hand, the short-term anomalies of precipitation may trigger extreme events such as floods and droughts, which exert profound impacts on the productivity and livelihoods of human society (Lenderink and Van Meijgaard, 2008; Akbari Asanjan et al., 2018). On the other hand, its long-term variations are closely linked to large-scale atmospheric circulation and potentially induce broader climatic changes (Bony et al., 2013; Huang et al., 2016). However, it still faces great challenges to reveal the complex physical process, influencing mechanisms and non-linear characteristics of precipitation due to the numerous factors

associated with precipitation occurrence and the existing uncertainties in current precipitation products compared to actual observations. (Morrison et al., 2020; Jian et al., 2022; Li et al., 2022; Zhao et al., 2024a). Therefore, combining limited observational data to clarify the key variables for precipitation retrieval and obtain high-quality precipitation dataset will inevitably help to address the above scientific issues (Jiang et al., 2023).

Precipitation data can be obtained primarily based on ground observation instruments and meteorological satellite retrieval (Skofronick-Jackson et al., 2017). Specifically, ground-based rain gauges are not only the most direct observational tool, but also have high measurement accuracy, which is widely used for the evaluation of satellite products (Gautam and Pandey, 2022; Zhu and Ma, 2022). However, they are confined to provide data from many single points, which limits the extrapolation of rainfall pattern over broader regions (Li et al., 2013b). Ground-based meteorological radars possess spatial

* Corresponding author at: College of Atmospheric Sciences, Lanzhou University, Lanzhou 730000, China.

E-mail address: lijiming@lzu.edu.cn (J. Li).

<https://doi.org/10.1016/j.atmosres.2025.108112>

Received 19 September 2024; Received in revised form 18 March 2025; Accepted 29 March 2025

Available online 5 April 2025

0169-8095/© 2025 Elsevier B.V. All rights are reserved, including those for text and data mining, AI training, and similar technologies.

representativeness within a certain area, but radar echoes are susceptible to interference such as beam blockage and non-meteorological echoes (Ye et al., 2015; Tan and Chen, 2023). Furthermore, the deployment density and cost of ground instruments also introduce large uncertainty to precipitation estimation (Dabberdt and Schlatter, 1996; Chen et al., 2022b). Compared to ground-based observations, satellite remote sensing can overcome above drawbacks, and the development of satellite-based precipitation retrieval algorithm will help to obtain precipitation products with large spatial coverage and long temporal effectiveness (Hou et al., 2014). Meteorological satellites are mainly classified into Low Earth Orbit (LEO) satellites and Geostationary Earth Orbit (GEO) satellites according to their operational orbit. Passive microwave sensors and precipitation radar carried by LEO satellites have the advantage of directly reflecting cloud particle information relevant to precipitation (Michaelides et al., 2009; Kidd et al., 2016). However, the spatial resolution of passive microwave sensors is very low, and precipitation radars have a relatively small scanning coverage. Moreover, due to the limitation of LEO satellite's operational orbit, passive microwave sensors and precipitation radars have a low sampling frequency and considerable scanning gaps in the same area, which prevents the capture of rapidly evolving storms and the continuous observation to the same precipitation event (Joyce et al., 2004). In contrast, GEO satellites equipped with visible and infrared (VIS/IR) sensors can provide near real-time and high-resolution observations, which play an irreplaceable role in monitoring heavy precipitation events at small scales with rapid spatiotemporal variations. In previous studies, some IR-based algorithms estimate precipitation by linking brightness temperature to surface rain rate, and the VIS channels can provide some information about cloud optical properties related to precipitation (Adler and Negri, 1988; Thies et al., 2008a). However, the VIS and IR radiations are limited to the cloud top and cannot penetrate cloud layers, and the statistical relationship between cloud top brightness temperature and surface rain rate is not always reliable, so the precision of precipitation retrieval still needs to be improved (Ebert et al., 2007). Precipitation products can also be obtained by inversion and fusion of active and passive satellite multi-sensor observations, such as the Global Precipitation Climatology Project (GPCP) (Huffman et al., 1997), the Global Satellite Mapping of Precipitation (GSMaP) (Okamoto et al., 2005), the TRMM Multi-Satellite Precipitation Analysis (TMPA) (Huffman et al., 2007) and the Integrated Multi-satellite Retrievals for the Global Precipitation Measurement (GPM IMERG) (Hou et al., 2014), which have been widely used for previous studies. Nevertheless, merged products cannot provide real-time data because of long delays (e.g., 3.5 months for IMERG Final Run). Moreover, due to the constraints of inherent physical assumptions and systematic errors in physical retrieval and merge methods, these precipitation products still suffer from low accuracy and some uncertainty in some cases (e.g., dry climate, light and heavy rainfall) (Prakash et al., 2016; Retalis et al., 2020; Tang et al., 2020; Li et al., 2021a; Ramadhan et al., 2022; Gavahi et al., 2023; Peinó et al., 2024).

Despite different precipitation products can be obtained by different retrieval methods, one thing is certain: as an important carrier of precipitation, cloud is closely related to the probability and intensity of precipitation occurrence, and dynamic and thermal conditions in the meteorological background field also play a crucial role in the formation and evolution processes of cloud and precipitation. Based on the above considerations, some studies have shown that a low cloud-top brightness temperature or distinct textural features can be employed to indicate deep convective precipitation events in tropical regions (Hong et al., 2004). Nakajima et al. (2010) noted that the retrieval of cloud effective particle radius using the 2.1- μm wavelength from satellite imagers has the potential to infer precipitation in warm water clouds. Cloud droplets with a larger particle radius are more inclined to fall against the updraft, and optically thick clouds with an extensive vertical extent can reduce evaporation and promote the substantial growth of cloud droplets during the falling process, consequently, such clouds are deemed more

likely to generate precipitation (Lensky and Rosenfeld, 2003; Nauss and Kokhanovsky, 2006). Chiu et al. (2014) pointed out that drizzling clouds have significantly higher geometric thickness and liquid water path than non-drizzling clouds. As for meteorological conditions, Brown and Zhang (1997) found that low mid-tropospheric humidity inhibits the development of deep convective cloud through dry air entrainment. Long et al. (2021) pointed out that precipitation events become more concentrated both temporally and spatially under higher temperature conditions. Rafati et al. (2024) noted that low-level wind shear can be served as a predictor for mean and maximum precipitation of mesoscale convective systems. These studies show that cloud properties and associated meteorological conditions should be taken into account for incorporating more precipitation-related processes (e.g. the evaporation during the raindrop falling process) in high-quality precipitation retrieval (Salamalikis et al., 2016; Chen et al., 2020). However, the relationship between precipitation and cloud properties, meteorological conditions, and cloud-top brightness temperature is usually highly non-linear, and traditional physically and statistically based precipitation retrieval methods often struggle to accurately resolve these non-linear problems (Hong et al., 2005; Ma et al., 2020; Zhou et al., 2022). Additionally, it is still unclear which variables should be emphasized in the precipitation retrieval algorithm.

With the rapid development of computer processing speed and storage efficiency, keywords like big data and machine learning have become prominent in numerous scientific domains (Wang et al., 2022b; Shang et al., 2024a; Shang et al., 2024b; Zhang et al., 2024). Some machine learning and deep learning methods, such as Random Forest (RF), XGBoost, Support Vector Machine (SVM), and Convolutional Neural Network (CNN), have advantages of handling large volume data and capturing non-linear relationships. They demonstrate robust generalization capabilities without the need for priori knowledge, and provide novel insights for addressing retrieval problems based on satellite remote sensing. For instance, Wei et al. (2021) estimated ground-level PM_{2.5} concentrations with a LightGBM model from the Himawari-8 satellite aerosol optical depth product, and the results were significantly better than those derived from traditional statistical methods. Yang et al. (2022) presented the potential of XGBoost for predicting cloud parameters using multi-spectral data from the Advanced Himawari Imager (AHI) onboard the Himawari-8 satellite. In the aspect of passive satellite-based quantitative precipitation estimation (QPE), machine learning methods are widely utilized as well. For example, Li et al. (2021a) made a preliminary attempt to reproduce three rainstorm cases in the Southeast of China using a random forest model combined with multi-source products from Fengyun-4 satellite (FY-4 A) and reanalysis data, and the results confirmed the potential of machine learning for applications in QPE. Wang et al. (2020) employed CNN for rainfall estimation over the Continental United States (CONUS) using Geostationary Operational Environmental Satellite (GOES) multi-band IR data, the results of which illustrate better performance than the operational product. Ma et al. (2022) proposed an artificial neural network framework named FY4QPE-MSA, driven by multispectral analysis (MSA) from FY-4 A AGRI, which can generate accurate QPE. In spite of the fact that many scholars have proposed various machine learning-based algorithms for the satellite QPE, challenges still persist due to poor interpretability associated with machine learning methods. For example, the selection of input variables during the training process is random and arbitrary, and the importance and the degree of information gain of different variables is not explicit, which hampers effective execution of operational applications. Additionally, the sensitive factors for precipitation under different environmental conditions are not well understood, and the dependency of precipitation on cloud types has not been further studied. Furthermore, the characteristic of highly-skewed and heavy-tailed hourly precipitation distribution poses problems for the application of machine learning in QPE (Koch and Naveau, 2015; Min et al., 2019).

As results, this study primarily focuses on the following three points:

(1) Using multiple machine learning methods, including Random Forest, XGBoost, and LightGBM to improve the accuracy of passive satellite precipitation estimations by considering various effective variables such as satellite spectral signals, meteorological parameters, and cloud properties, and adjusting the distribution of hourly precipitation from ground observations by adopting sample balance and natural logarithm transformation. (2) Taking different combinations of the satellite level-1 VIS/IR data, cloud property product, meteorological conditions and other ancillary variables (e.g., longitude, latitude and time) as inputs, conducting multiple sensitivity tests to confirm their importance for precipitation estimations and identify which variables are more effective to high-precision precipitation estimation. (3) Comparing the algorithm's estimation results with the GPM level-3 IMERG under different climatic regions and cloud types to identify consistencies and differences and further analyze the underlying reasons of differences between datasets. The results of this study are expected to provide valuable references for the development of future precipitation retrieval algorithms in the aspect of data processing, variable selection under different environmental conditions and technical improvements for specific cloud types. The structure of this paper is organized as follows: the data used in this study are introduced in Section 2. Section 3 describes the methodology used. Section 4 shows the performance of the QPE algorithm and evaluates it from multiple perspectives. The conclusions are presented in Section 5.

2. Data

2.1. Study area and Ground-based precipitation observation

In this paper, we selected the overlapping region of the mainland China and the scan coverage of the Himawari-8 satellite as the study area, located between 80°–136°E and 15°–54°N. As shown in Fig. 1, the background color represents digital elevation model (DEM) data. It can be observed that the terrain in China is complex, with an elevation that gradually decreases from west to east, presenting a stepped distribution. In addition, the climate, monsoons and precipitation in mainland China shows distinct regional and seasonal characteristics because of the topography influence (Jin et al., 2021). In consideration of this, the research area was classified into four regions: arid, semi-arid, semi-humid, and humid regions based on aridity index (AI) (Feng and Fu,

2013).

High-quality hourly precipitation records from more than 2400 ground-based meteorological stations are preserved in the National Meteorological Information Center (NMIC) of the China Meteorological Administration (CMA). Strict quality controls are implemented during data compilation process, ensuring excellent data quality and completeness. The annual average rates of missing data and errors are low, and the accuracy is very high (Lei et al., 2022). In this study, the ground-based precipitation observation was introduced as training labels. Fig. 1 showed the distribution of these stations, which cover a significant portion of mainland China. The station density is notably high in the eastern and southern humid regions, but relatively sparse in the western and northern arid regions, especially in the Tibetan Plateau, and this distribution may bring a significant impact on the performance of the algorithm in different climatic regions. It is worth noting that owing to sensitivity limitations of the instruments, the minimum recorded rain rate is 0.1 mm/h, which is used as the threshold to differentiate between precipitation and non-precipitation pixels.

2.2. Himawari-8 Satellite Level-1 spectral data

The Himawari-8 GEO satellite was launched in 2014 and operates at 140.7°E above the equator. The satellite is equipped with the Advanced Himawari Imager (AHI), which provides full-disk scan data with temporal and spatial resolutions ranging from 2.5 to 10 min and 0.5 to 2 km at the nadir point, respectively. The AHI comprises 16 spectral channels, including three visible, three near-infrared, and ten infrared channels, with center wavelengths spanning 0.47 to 13.3 μm (Letu et al., 2020; Letu et al., 2023). Further details can be found on the Japan Aerospace Exploration Agency (JAXA) website (<https://www.data.jma.go.jp/m-scweb/en/index.html>).

The Level-1 products derived from multi-spectral observations of the AHI provide diverse information closely associated with precipitation. In theory, the brightness temperature at approximately 11 μm is utilized to extract cloud-top temperature. Hong et al. (2004) used the 10.7 μm channel cloud features from satellite imagery to construct the Precipitation Estimation from Remotely Sensed Information using Artificial Neural Networks Cloud Classification System (PERSIANN-CCS), which is widely recognized as one of the global precipitation datasets. The positive brightness temperature difference between water vapor and

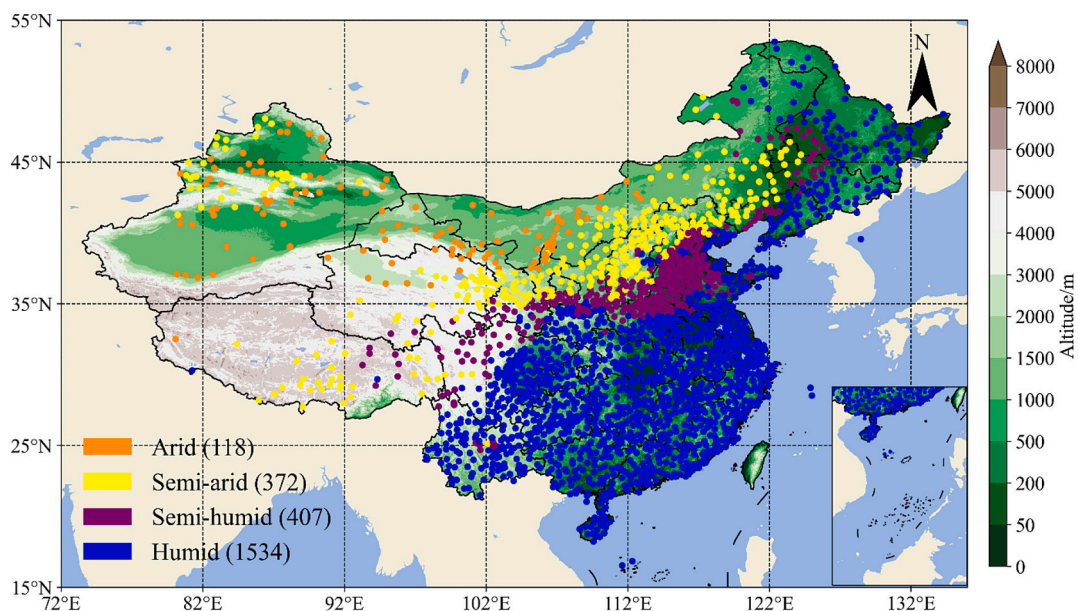


Fig. 1. Rain gauges and surface elevation distribution in the study area at 10:00, on May 13, 2016. The color of dots represents the corresponding climate zones, and the number of rain gauges for each zone is shown in parentheses.

infrared channels (WV-IR) can be served as an indicator of deep convective clouds (Schmetz et al., 1997; Thies et al., 2008a, 2008b). The VIS/NIR band such as approximately 0.6 μm can provide information about cloud optical thickness, and the 1.6–3.9 μm channel is applied to represent information about the cloud effective particle radius at different penetration depths (Platnick, 2000; Chang and Li, 2002; Kühnlein et al., 2010; Letu et al., 2020). These cloud optical parameters are utilized to identify rainfall from stratiform precipitation clouds commonly observed in mid-latitude regions. Thies et al. (2008a, 2008b) utilized infrared brightness temperature differences (3.9–10.8 μm , 3.9–7.3 μm , 8.7–10.8 μm , 10.8–12.1 μm) to delineate nighttime precipitation areas. The underlying principle is that higher cloud water path is usually associated with precipitating clouds, and the product of optical thickness and particle size has a functional relationship with cloud water path (Minnis et al., 2011). These four brightness temperature differences can be used to qualitatively estimate the cloud optical thickness and particle size during nighttime. Among them, the 8.7–10.8 μm and 10.8–12.1 μm brightness temperature difference can provide additional cloud-top particle phase information (Baum et al., 2000). In fact, Behrangi et al. (2009) indicated that the performance of the QPE algorithm significantly improves with an increasing number of input satellite channels. Therefore, in this study, to incorporate as much precipitation-related information as possible and demonstrate which spectral channels are more effective for precipitation retrieval, we utilized the full spectral data from the AHI Level-1 product, including VIS channels for bands 1–6, IR channels for bands 7–16, some brightness temperature differences, and angle parameters. In order to add cloud texture feature information, the cloud-top brightness temperature gradients (BT_G) of band 13 and band 14 are also introduced into the algorithm, which is expressed as follows (Li et al., 2021a):

$$BT_G = \sqrt{[BT(i-1, j) - BT(i+1, j)]^2 + [BT(i, j-1) - BT(i, j+1)]^2} \quad (1)$$

where BT is the brightness temperature from band 13 and band 14; and i , j represent the pixel position in the satellite image. A high BT_G indicates sharp changes in temperature over a small horizontal distance, which usually suggests the presence of convective systems (Bedka et al., 2010; Sun et al., 2019). The temporal resolution for all the mentioned data is 10 min, and the spatial resolution is 5 km (see Table S1).

2.3. NASA SatCORPS Himawari product dataset

The NASA SatCORPS Himawari product dataset contains cloud property data from Himawari observations, which was provided by NASA Langley's Satellite Cloud and Radiation Property Retrieval System (SatCORPS). Compared to the Himawari-8 official Level-2 cloud property product, this data maintains a high level of quality and complements more cloud physical and radiative properties. In this study, several cloud parameters derived from this product were collected, including Liquid or Ice Water Path (LWP_IWP), Cloud Top Pressure (CTP), Cloud Bottom Pressure (CBP), Cloud Effective Particle Radius (CER), Cloud Top Temperature (CLTT), Cloud Bottom Temperature (CLBT), Cloud Top Height (CLTH), Cloud Bottom Height (CLBH), Cloud Phase (CP), and Cloud Optical Depth (COD). The detail information of these variables is shown in Table S1. More information is available on the website (<https://satcorps.larc.nasa.gov>).

2.4. ERA5 reanalysis dataset

The ERA5 is a state-of-the-art reanalysis dataset developed by the European Centre for Medium-Range Weather Forecasts (ECMWF). It contains a variety of meteorological background field parameters with a high spatial and temporal resolution (1 h and $0.25^\circ \times 0.25^\circ$). Single level meteorological parameters such as K index, convective available potential energy (CAPE), total column water (TCW) and evaporation, as well as parameters such as temperature (T) and relative humidity (RH)

at different pressure levels were introduced as input. Parameters like CAPE and K index indicate the potential for the development of convective systems or thunderstorms. Other parameters like T and RH profile complement the dynamics and thermal conditions for the cloud generation and development, which can further enhance the performance of QPE algorithms (Min et al., 2019). The detail information of these variables is outlined in Table S1.

2.5. GPM IMERG precipitation dataset

The GPM mission is a global network of satellites designed for detection and monitoring of precipitation and snow. Serving as the successor to the TRMM, the GPM constellation includes the GPM Core Observatory LEO satellite equipped with an advanced GPM Microwave Imager (GMI) and Dual-frequency Precipitation Radar (DPR), along with several partner satellites. The Integrated Multi-satellitE Retrievals for GPM algorithm (GPM IMERG) integrates multi-source information, including microwave precipitation analysis from active satellites, infrared precipitation estimation from passive satellites and gauge precipitation data. As a widely applied precipitation product, GPM IMERG exhibits higher quality and accuracy compared to most reanalysis, satellite, or merged gridded precipitation products and performs well across different spatiotemporal resolutions, which provides crucial support for scientific research on precipitation (Tang et al., 2016; Prakash et al., 2018; Tang et al., 2020; Nascimento et al., 2021; Moazami and Najafi, 2021; Peinó et al., 2022; Pradhan et al., 2022). The IMERG Final-Run product is adjusted using the GPCC gauge analysis and offers a more reliable precipitation estimation compared to Early Run and Late Run (Wang et al., 2017). It is also the recommended product for research on the official website. To evaluate the performance of the QPE algorithm developed in this study, we selected the IMERG Final Run version 07 product as a comparison object, with spatial grids of $0.1^\circ \times 0.1^\circ$ and a temporal interval of half an hour.

3. Methodology

The proposed algorithm structure for passive satellite QPE based on multiple machine learning models in this study is depicted in Fig. 2. The entire flowchart primarily consists of three segments: (a) Inputs and reference, including data preprocess for temporal synchronization, spatial matching, dataset partition, sample balance and natural logarithm transformation. (b) Machine learning algorithms, which includes model construction and parameter fine-tuning. (c) Validation and evaluation, which involve that the algorithm performance is demonstrated based on the independent validation dataset and compared with the GPM data.

3.1. Data preprocessing

Due to a relative higher frequency of warm-season precipitation events and the limitation on rain gauge data volume, the temporal range of all data used in this study spans from May to September in the years 2016 to 2018 and from May to July in 2019. Satellite visible channel data and cloud optical property product (such as cloud optical depth) are only available when the sunlight appears, so we selected the daytime period from 10:00 to 16:00 (CST), during which both of them can cover the whole study region. To achieve fine-scale precipitation estimation, ERA5 data and NASA SatCORPS Himawari cloud product were resampled to a 5 km resolution, which is consistent with satellite spectral data. It should be noted that the GPM product is not resampled, but remains its original resolution. Resampling the GPM may introduce additional errors and reduce its evaluation metrics as a comparison product. Considering that the ground precipitation data is hourly level, the 10-min interval observation from Himawari-8 was averaged within each hour and the GPM product was also sampled at hourly intervals. After integrating all input variables, a nearest-neighbor method was used to

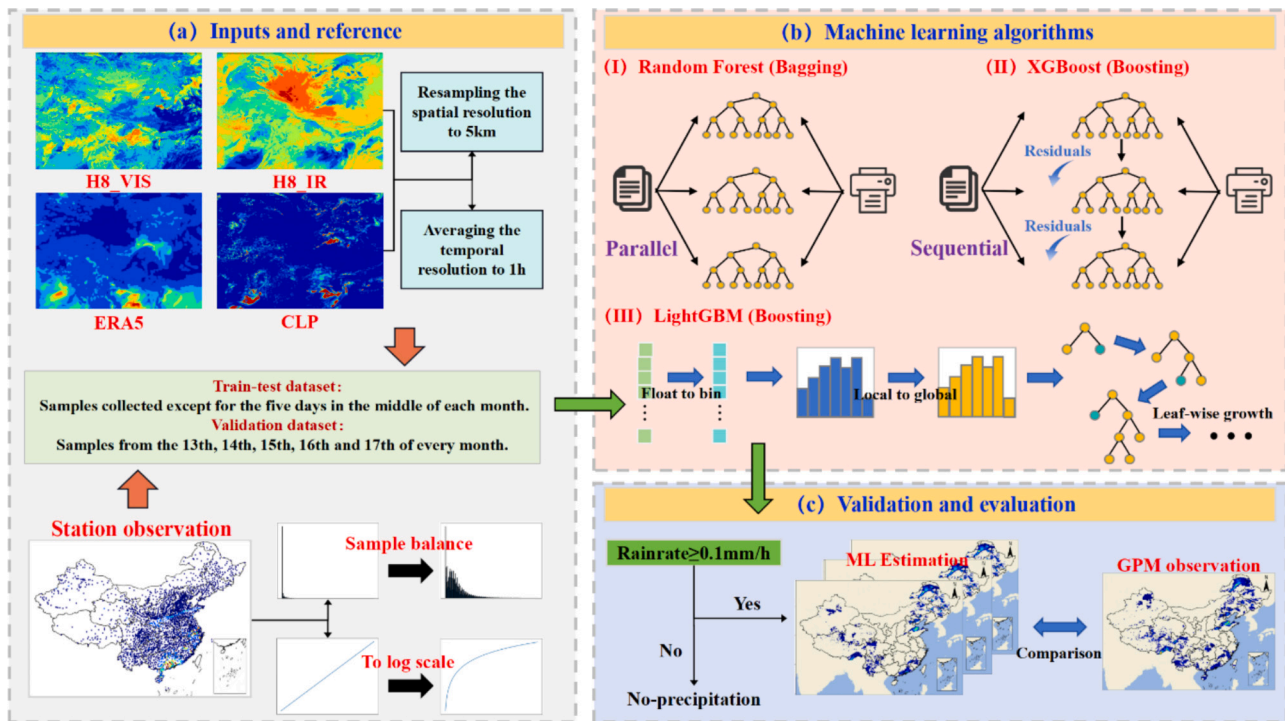


Fig. 2. Flowchart of the proposed quantitative precipitation estimation algorithm. (a) The preprocessing of input and reference data. (b) The structure of three machine learning models. (c) The validation and comparison between algorithm estimation and GPM IMERG.

interpolate all grid data to station data. To implement applications with near real-time prediction, the matching of ground precipitation and input variables is delayed by one hour. (i.e., the input variables at the $t-1$ moment are matched with the precipitation at the t moment).

High-quality training ground truth (station observation precipitation in this study) plays a crucial role in the construction of machine learning (ML) algorithms. A key challenge for ML-based QPE algorithms is the scarcity of precipitation samples, as well as the heavy-tailed and highly-skewed distribution of rain rate (Min et al., 2019; Wang et al., 2020). To mitigate this issue, we implemented three strategies. Initially, we balanced precipitation and non-precipitation samples. The original sample ratio was approximately 1:10, and we removed non-precipitation samples by performing down-sampling to achieve a ratio of approximately 1:1. Subsequently, we applied down-sampling to the light precipitation samples to alleviate the exponential decay trend of sample number from light to heavy rain rate. Sample balance enables the model to focus more on precipitation events and increases the relative weight of heavy precipitation events in the algorithm. Furthermore, we performed a natural logarithm transformation. This process offers two benefits: firstly, it narrows down the range of the training label values, which can remarkably lighten the influence of heavy-tailed distributions on the algorithm robustness. Secondly, the sample balance procedure inevitably alters the original distribution of rain rate, leading model to become excessively sensitive to larger values. The natural logarithm transformation helps amplify the differences among light rain rate values, allowing the model to perceive and learn subtle variations more easily within these data (Peng et al., 2022).

As a prominent model for big data, machine learning leverages the input of high-dimensional feature variables as a primary advantage, but the importance and the degree of information gain of the input variables on precipitation estimations is still open to debate. To elucidate the rationality of the input data, we conducted multiple experiments with different input combinations and validated the performance. All samples utilized for experiments were divided into training, testing, and validation datasets. For the sake of assessing the model's generalization capability, data from the middle five days of each month (from the 13th

to the 17th) were extracted as an independent validation dataset, which is unrelated to the model training process. The remaining samples were randomly divided in a 4:1 ratio, with 80 % used to construct the training dataset and 20 % allocated for hyper-parameter tuning as the testing dataset. After these steps, the training, testing, and validation dataset collectively contain 186,735, 46,684, and 1,535,146 samples, respectively.

3.2. Model construction

We employed three machine learning methods, including Random Forest (RF), XGBoost, and LightGBM. These methods all belong to the category of ensemble learning based on multiple decision trees, and their outstanding performance has been widely validated in many practical applications (Min et al., 2020; Wei et al., 2021; Chen et al., 2022a, 2022b). The core concept of RF is Bagging (bootstrap aggregating), which involves the following steps: Firstly, n times random sampling with replacement are drawn from the training dataset to form n sub-training datasets; Secondly, every decision tree is trained using the aforementioned sub-training dataset; Thirdly, the predictions of all decision trees are combined using a voting method to generate the final prediction. The strategy of randomly selecting features at each node introduces randomness into all the decision trees within the RF, thereby enhancing the model's stability and generalization ability (Breiman, 2001). In contrast, XGBoost and LightGBM are based on the concept of Gradient Boosting, which involves iteratively updating weights based on the residuals of the previous training round, and the weighted predictions of each weak classifier are combined to obtain the final result (Chen and Guestrin, 2016; Ke et al., 2017). LightGBM incorporates optimization strategies such as leaf-wise growth, histogram-based algorithm, exclusive feature bundling, and memory optimization, which significantly improve the training speed (Wei et al., 2021).

Bias and variance are crucial factors that affect ML algorithm performance. When the bias is large, the large gap between the predictions and the references suggests that the structure of the model maybe too simple, and underfitting will occur. Conversely, a significant variance

means that the model tends to overly adapt to the training dataset but fails to achieve satisfactory performance in the other datasets, indicating poor generalization or overfitting. In general, it is difficult to minimize both bias and variance simultaneously, and there is a relationship between them, which is recognized as the bias-variance tradeoff (Lin et al., 2022). Parameter tuning can help work out the aforementioned issues to some extent. Some important parameters, such as $n_estimator$, represent the number of decision trees. Increasing this value can reduce the bias and improve performance, but it may also lead to excessively high computational costs and overfitting. The parameter max_depth signifies the maximum depth of each decision tree. An overly high max_depth may increase model complexity and result in overfitting and prolonged training time. While a low max_depth can simplify the model but may potentially cause the consequence of underfitting. The $learning_rate$ in XGBoost and LightGBM controls the contribution degree for each decision tree. A small value can enhance the algorithm's generalization ability, but requires an increased number of iterations during the training process. In the random forest, $max_features$ denotes the number of features considered when splitting each node, which can effectively reduce the risk of overfitting. The main hyperparameter settings mentioned above are detailed in Table 1.

Traditional QPE algorithms usually identify precipitation pixels and subsequently estimate precipitation rate (Min et al., 2019; Zhu and Ma, 2022). These two-stage models inevitably introduce the error of identification into the estimation process. In order to build an algorithm that combines precipitation identification and estimation segments, in the output stage, the estimation results less than 0.1 mm/h are automatically classified as no precipitation by our model, which is consistent with the observation threshold of rain gauge.

3.3. Evaluation metrics

Six commonly used binary forecast evaluation metrics and three regression forecast metrics were introduced to comprehensively illustrate the algorithm capabilities in precipitation identification and estimation: probability of detection (POD), false alarm ratio (FAR), accuracy rate (ACC), critical success index (CSI), Heidke skill score (HSS), equitable threat score (ETS), Pearson correlation coefficient (R), mean absolute error (MAE), and root mean square error (RMSE), which are calculated by the following formulas:

$$POD = \frac{P_1}{P_1 + P_2} \quad (2)$$

$$FAR = \frac{P_3}{P_1 + P_3} \quad (3)$$

$$ACC = \frac{P_1 + P_4}{P_1 + P_2 + P_3 + P_4} \quad (4)$$

$$CSI = \frac{P_1}{P_1 + P_2 + P_3} \quad (5)$$

$$HSS = \frac{2(P_1P_4 - P_2P_3)}{(P_2^2 + P_3^2 + 2P_1P_4 + (P_2 + P_3)(P_1 + P_4))} \quad (6)$$

$$ETS = \frac{P_1 - Dr}{P_1 + P_2 + P_3 - Dr}, Dr = \frac{(P_1 + P_2)(P_1 + P_3)}{P_1 + P_2 + P_3 + P_4} \quad (7)$$

$$R = \frac{\sum_{i=1}^n (O_i - \bar{O})(P_i - \bar{P})}{\sqrt{\sum_{i=1}^n (O_i - \bar{O})^2 \sum_{i=1}^n (P_i - \bar{P})^2}} \quad (8)$$

$$MAE = \frac{1}{n} \sum_{i=1}^n |O_i - P_i| \quad (9)$$

$$RMSE = \sqrt{\frac{1}{n} \sum_{i=1}^n (O_i - P_i)^2} \quad (10)$$

where P_1 is the number of samples for which both observation and prediction indicate precipitation; P_2 is the number of samples for which observation indicates precipitation while prediction indicates non-precipitation; P_3 represents the number of samples for which observation indicates non-precipitation while prediction indicates precipitation; P_4 represents the number of samples for which both observation and prediction indicate non-precipitation; n represents the total number of samples; O_i represents the i^{th} ground observation, and P_i represents the i^{th} estimation. A detailed description of these evaluation metrics can be found in Appendix.

3.4. Shapley Additive Explanations (SHAP) analysis

SHAP is a method for interpreting the predictions of machine learning models, the core idea of which is based on the theory of Shapley values in game theory (Peng et al., 2023). It not only allows for global interpretability by summarizing the impact of each feature across the entire dataset, but also provides detailed explanations for individual predictions. Additionally, SHAP is also able to provide the positive or negative contributions on the prediction for different features. The SHAP value can be calculated based on Eq. (11):

$$\varphi_i = \sum_{S \subseteq N \setminus \{i\}} \frac{|S|!(|N| - |S| - 1)!}{|N|!} [f(S \cup \{i\}) - f(S)] \quad (11)$$

where φ_i is the Shapley value for feature i ; N is the set of all input features; S is a subset of N that does not include i ; $|S|$ is the number of features in S ; $|N|$ is the total number of features; $f(S)$ represents the prediction of the model when only the features in subset S are considered; and $f(S \cup \{i\})$ represents the prediction of the model when the features in subset S and feature i are considered. This calculation can be conveniently implemented by the Shap library in Python.

4. Results and discussion

4.1. Analysis of the importance of input features on precipitation estimations

The preceding Section 2 indicates that all considered input data are closely associated with the processes of cloud and precipitation formation and evolution, yet their importance and the degree of information gain on precipitation estimations remains unclear. To further analyze this issue comprehensively, tests with different combinations of inputs for three machine learning (ML) models were conducted based on the independent validation dataset, and the input schemes and evaluation metrics are presented in Table S2. It can be observed that ML models perform best when all variables are included as inputs. Although the ERA5 + IR experiment has the highest POD value among ML models, it also has a larger FAR, indicating a higher likelihood of misclassifying non-precipitation as precipitation. From the perspective of single type

Table 1

The main hyperparameter values used for machine learning models in this study.

Model	Hyperparameter	Value
Random Forest	$n_estimators$	300
	max_depth	20
	$max_features$	Sqrt
	$feature_fraction$	0.9
LightGBM	num_leaves	100
	$learning_rate$	0.05
	$n_estimators$	300
XGBoost	$learning_rate$	0.05
	max_depth	10

variables, ML models perform best with VIS data as input, followed by cloud property data, with a relatively poor performance for IR data, and the worst for ERA5 data, which indicates that the visible channels and cloud properties contain more gain information, and are key to accurate estimation of precipitation. Ablation tests in the last four rows of each model further confirm the above importance ranking. When four types of variables are eliminated in turn, the ACC, CSI, HSS, ETS and R values experience the most significant decline when VIS data is removed and the least decline for R when ERA5 data is excluded. It is worth noting that the decline in these metrics when cloud property data is removed is very close to that when IR data is removed, potentially due to the fact that the retrieval of some cloud parameters primarily utilizes VIS channels, where part of the redundant information of cloud property data preserved in VIS data compensates for the influence of information removal (Letu et al., 2019). The middle six tests in each model in Table S2 show a significant enhancement in these metrics when compared to models trained solely with a single type of variables, which suggests that complementary relationships between different variables, and all types of variables are beneficial to the improvement of algorithm performance. These results emphasize the necessity of incorporating cloud properties, VIS/IR information as inputs and the rationality of utilizing meteorological background field parameters as supplementary information in the ML QPE algorithm, despite potential negative influences from solar irradiance, satellite observation angles, and data inversion errors. Given that the optimal results from the “ALL” test experiment, subsequent discussions are based on this scheme.

To represent the contribution of input variables to the algorithm, Table S3 provides the feature importance scores ranking for different variable types. The feature importance score is obtained using embedded calculation methods within the three ML frameworks. Basic input variables such as time, longitude, latitude and angle information are excluded from this ranking. It is evident from the ranking that the VIS data consistently holds high positions, almost always appearing in the top 20, which indicates that VIS variables have the most significant contribution to the algorithm. The adjacent band 07 shortwave infrared channel also has a relatively high ranking. The infrared brightness temperature difference and cloud top temperature gradient also rank highly, these parameters can reflect cloud top state and texture characteristics (Ba and Gruber, 2001; Hong et al., 2004; Zhu and Ma, 2022). Among the ERA5 background field variables, CAPE and K index represent the development of convective energy and thunderstorm potential, respectively, which achieve high rankings as they are directly related to the dynamical processes of cloud and precipitation development (Yang et al., 2018; Wu et al., 2024). In cloud property variables, LWP-IWP and CLOT are concurrently ranked first and second across all three models, which indicates that they have the highest influence and substantial contributions to the precipitation estimation. Although other variables such as wind shear and macro-physical cloud characteristics receive lower feature importance scores, their role as auxiliary variables still exerts a non-negligible impact on the improvement of the algorithm. In summary, this ranking is generally consistent with the results of the tests in Table S2 to a certain extent, and effectively reflects the contributions of different variables to the algorithm.

4.2. Overall assessment

After determining the optimal input combination through sensitivity tests, we investigated the consistencies and differences in the performance of three ML models and GPM IMERG, which has been widely used as a comparison object in previous studies. It should be noted that all conclusions are based on the validation dataset. The evaluation metrics are comprehensively presented in Table 2, which utilize the ground gauge observations as a reference. When evaluating a model's precipitation identification capability, a high-performing model should combine a low probability of misclassification with the ability to correctly identify a greater number of precipitation events. Fig. S1 depicts their confusion matrix. It can be found that the LightGBM model has the best precipitation event identification capability among three models, with a relative high number of correctly identified precipitation events and the least misclassification samples in the confusion matrix, resulting in the CSI value of 0.492, HSS value of 0.623 and ETS value of 0.452. It correctly distinguishes precipitation and non-precipitation events with a probability of 93 %. Although the RF model has the highest number of correctly identified precipitation samples, this comes at the expense of high false alarm (see Fig. S1(c)). Compared to the GPM product with the POD of 0.601 and FAR of 0.548, the LightGBM model combines efficient precipitation identification (POD increased by 0.23) and low-probability false predictions (FAR decreased by 0.095). The regression evaluation metrics in the last three columns of Table 2 are used to evaluate the performance of precipitation rate estimation. The results show that the LightGBM model has the R value of 0.559, MAE of 0.214 mm/h, and RMSE of 1.186 mm/h. Although the XGBoost model possesses slightly higher R and lower RMSE compared to LightGBM, the LightGBM model significantly outperforms XGBoost in terms of training time because of its embedded optimization strategies. The GPM product shows a lower R (around 0.4) and higher MAE and RMSE compared to ML models. A large part of the disadvantage observed in GPM metrics may be attributed to its high misjudgment rate for true precipitation events (see Fig. S1(d)). Although the RF model has the lowest RMSE, it should be treated with caution due to its weakness in estimating heavy precipitation, which will be shown in the following part. Fig. 3 and Fig. S2 show the scatter density plots of the model estimations based on the test and validation datasets against ground observations, respectively. The color intervals on the logarithmic scale are used to represent the Gaussian kernel density of sample points. The overall distribution of the scatters in the independent validation dataset estimation is similar with that in the test dataset, but still shows significant differences. The gap is primarily attributed to the difference in sample distributions between the two datasets. The samples in the test dataset are obtained by sample balance processing according to the number of precipitation and non-precipitation events and the number of samples within each precipitation intensity interval, whereas the independent validation dataset retains a large number of non-precipitation and light precipitation samples, which preserves the heavy-tailed and highly-skewed characteristic of the original distribution. Additionally, the ML parameter tuning procedure may cause overfitting, which is another reason for the discrepancy between Fig. 3 and Fig. S2. In the test dataset (Fig. S2), the R values of three ML models all exceed 0.6, and most points below 10 mm/h are concentrated around the 1:1 line, indicating that ML-based algorithms perform well in estimating precipitation within this intensity

Table 2

Summary of evaluation metrics for the optimal LightGBM (LGB), XGBoost (XGB), Random Forest (RF) and GPM-IMERG (GPM).

Model	POD	FAR	ACC	CSI	HSS	ETS	R	MAE (mm/h)	RMSE (mm/h)
LGB	0.831	0.453	0.930	0.492	0.623	0.452	0.559	0.214	1.186
XGB	0.835	0.463	0.928	0.486	0.616	0.445	0.563	0.214	1.165
RF	0.856	0.506	0.916	0.456	0.583	0.412	0.538	0.215	1.155
GPM	0.601	0.548	0.908	0.347	0.466	0.304	0.4	0.225	1.287

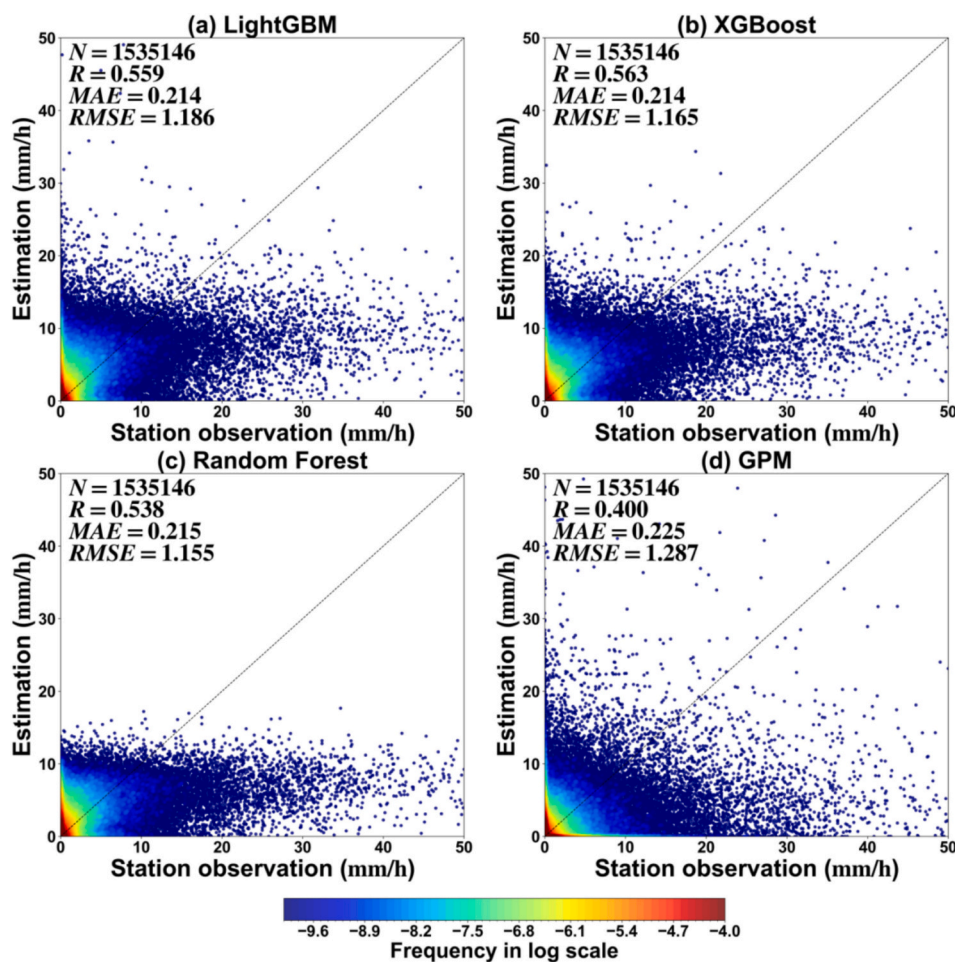


Fig. 3. Comparison of precipitation estimation results based on the validation dataset against rain gauges for (a) LightGBM, (b) XGBoost, (c) Random Forest and (d) GPM-IMERG.

range. However, there is a noticeable underestimation for precipitation exceeding 15 mm/h, which may be related to the fewer training samples of heavy precipitation (Min et al., 2019; Li et al., 2021a; Yang et al., 2023). Additionally, when heavy rainfall occurs, the trend that precipitation increases along with cloud water path becomes less significant, or even stops increasing, which can be referred to as a saturation phenomenon (Horváth and Davies, 2007; Lazri and Ameer, 2016). The RF model shows the most severe underestimation (Fig. S2(c)), which is also a major contributing factor to its lower R value. In the validation dataset (Fig. 3), a considerable number of precipitation events are missed by the GPM product, and the precipitation intensity of these events can even approach 20 mm/h (i.e., the bright line on the x-axis in Fig. 3(d)). In contrast, three ML models relatively alleviate this situation. Additionally, ML models perform better in estimating precipitation in the range of 0–10 mm/h compared to the GPM, and they also reduce the underestimation of precipitation exceeding 20 mm/h. It is important to note that the performance of the XGBoost and LightGBM models is similar, but the RF model differs significantly from both of them (Fig. 3(c)). The maximum estimation of the RF model is only about 19 mm/h, suggesting that it does not have the ability to estimate heavy precipitation in this study. We attribute this result to the fundamental differences between different ML algorithm principles. Despite the training dataset has been treated with sample balance, the proportion of heavy precipitation samples is still very limited. The RF model may have difficulty learning information about heavy precipitation through the training method of randomly selecting a subset of samples. In contrast, the XGBoost and LightGBM models are iteratively trained based on the residuals of the

previous layer, and the prediction weights of the next layer are updated by correcting the prediction errors of the previous one, which helps them to improve their estimation ability of heavy precipitation. Considering that GPM IMERG Final-Run has been adjusted at a monthly scale using GPCC gauge analysis, Fig. S3 supplies the performance of three ML methods and GPM at the monthly scale. Due to the limitations of the validation dataset samples, we used the average values in a month at each station over the study period for analysis. Overall, although the R value of GPM is still slightly lower than that of ML methods, its MAE and RMSE are relatively better, which can be attributed to its monthly scale adjustment.

4.3. Spatiotemporal performance analysis

To comprehensively analyze the performance of models and product across different regions, the spatial distributions of three evaluation metrics (R, RMSE, and CSI) based on gauge observations for three ML models and the GPM product in the independent validation dataset are shown in Fig. 4. It is evident that in the densely observed southeastern region with a humid climate, almost all sites achieve an R value exceeding 0.6 (Figs. 4(a), (b) and (d)). Among these, the XGBoost and LightGBM models perform slightly better than RF. Although the GPM product also has achieved good performance in the humid region, it still performs worse than ML models. As the location of stations extends towards the northwest, the density of the stations becomes sparser, and both the performance of ML models and the GPM product become worse. In the northwest arid region, ML models exhibit the poorest

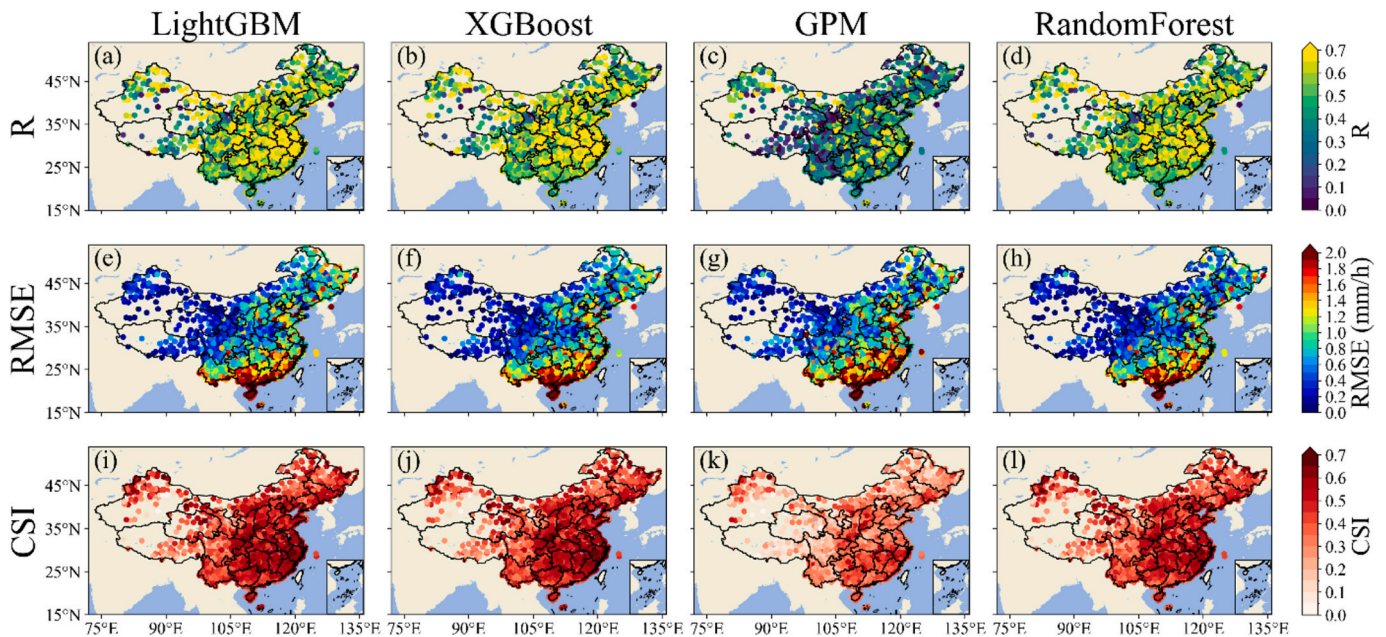


Fig. 4. Spatial distribution of evaluation metrics against ground rain gauges in the validation dataset.

performance, with many sites showing correlation coefficients below 0.2. This poor performance is attributed to the sparse station density and the limited quantity of precipitation samples in the training dataset, making it challenging for ML models to learn the relationship between ground precipitation and input features in this region. Additionally, You and Liu (2012) noted that the correlation between total water path and surface rain rate is lower in the arid region, which may have a greater impact on the performance of ML models that are most sensitive to cloud water path. Similarly, the GPM observation is also poorest in the northwest region, possibly due to its limitation in detecting light precipitation events, which occur frequently in arid areas (Li et al., 2021a). The spatial distribution pattern of CSI is similar with that of R, which is higher in the southeast and lower in the northwest (Figs. 4 (i)-(l)). In terms of RMSE in Figs. 4(e)-(h), both ML models and the GPM product exhibit a decreasing trend from the southeast to the northwest, which is related to the precipitation regional climatology (Shen and Xiong, 2015). Additionally, a significance test ($p < 0.01$) is conducted for the R of all stations (not shown). The results show that over 98 % of the stations in ML models pass the significance test, compared to less than 92 % of stations in GPM, which demonstrates that the precipitation estimations from ML models have a statistically stronger correlation with ground observations. Fig. 5 summarizes the overall metrics of all stations in different climatic regions, where a larger value of the arid index (AI) represents a wetter region, and a smaller value represents a drier region. In general, the CSI increases with AI, and the LightGBM model has the highest CSI in each region, indicating the most accurate precipitation identification in these datasets (Fig. 5(c)). In terms of precipitation estimation, the XGBoost model has R and RMSE that are quite similar with those of LightGBM (Fig. 5(a) and (b)), but its computational efficiency is significantly lower. Although RF's evaluation metrics are also pretty good, it significantly underestimates heavy precipitation events, as mentioned in Section 4.2. The R value of the LightGBM model is improved by 0.12, 0.21, 0.22 and 0.15, and the RMSE (unit: mm/h) is reduced by 0.01, 0.05, 0.13 and 0.11 compared to the GPM product in the arid, semi-arid, semi-humid, and humid regions, respectively. The significant improvement of the LightGBM model in the semi-arid and semi-humid regions may be attributed to its excellent performance in estimating moderate rain rate.

To further verify the accuracy of the GPM product and ML models, we selected the precipitation events occurred at September 16, 2018,

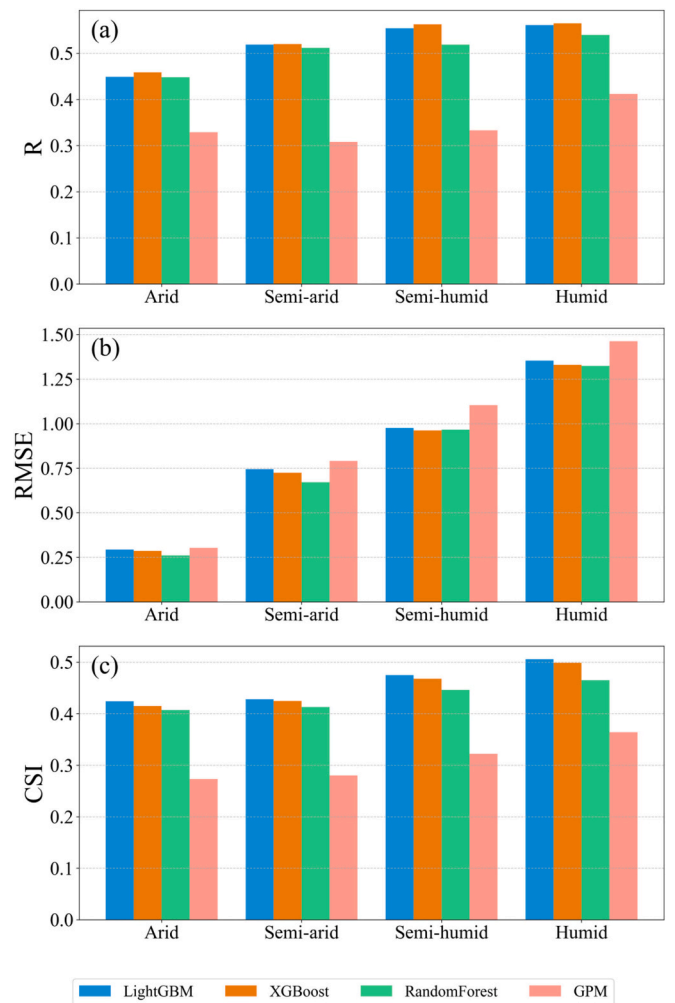


Fig. 5. Summary of (a) R, (b) RMSE and (c) CSI in different climatic regions for LightGBM, XGBoost, Random Forest and GPM-IMERG.

13:00 as a case study. This specific precipitation case impacted multiple provinces, including both moderate precipitation samples extending from central to eastern China and heavy precipitation samples induced by a typhoon in the southeastern region, as observed in Fig. 6. At first glance, both ML models and the GPM observation provide accurate boundary of the general precipitation distribution. The rainfall areas of three ML models are quite similar, but difference still exists in some regions. In terms of precipitation identification, ML models align more closely with ground observation, especially in accurately depicting the general outlines of the two concentrated precipitation areas. However, some subtle precipitation areas are missed by either ML models or GPM product, such as the northwestern part of Hubei Province (red region in Fig. 6(a)) and the central part of Shaanxi Province (blue region). ML models also misidentify some areas without precipitation, such as the central and southern parts of Jiangxi Province (grey region), Hainan Province (magenta region), and the western part of Yunnan Province (black region). As for rain rate estimation, the RF and XGBoost models notably underestimate rain rate exceeding 10 mm/h, whereas LightGBM outperforms them. All three ML models overestimate the rain rate in the coastal areas along the border of Zhejiang (cyan region) and Fujian (pink region). For the GPM product, there is a slight overestimation of moderate precipitation in the central of China. In the southeastern region, it exhibits some slight misjudgments regarding the intense precipitation center associated with convective system. In the western and northern regions of the Qinghai-Tibet Plateau, noticeable difference exists between ML models and the GPM product. However, their performance in this area can not be determined due to the lack of ground observation as a reference. To investigate whether the Qinghai-Tibet Plateau (TP) have experienced actual precipitation during this event, we introduced several satellite, reanalysis, and merged gridded precipitation products, including MSWEP-V2, CMORPH-CDR, TPhIPr and ERA5-Land (Xie et al., 2017; Beck et al., 2019; Muñoz-Sabater et al., 2021; Jiang et al., 2023). These precipitation products exhibit outstanding performance, especially TPhIPr, which is specifically designed for application in the TP region. Fig. S4 presents the cloud water path (CWP) distribution and precipitation estimations from the above products. It can be seen from Fig. S4 (b) that there is an obviously high-value of CWP over the TP. Given that CWP (lwp_{iwp}) consistently ranks as the most influential predictor in ML models (Table S3), ML models are more likely to predict precipitation over the TP in this event. Similarly, the other precipitation products also exhibit a discontinuous precipitation distribution over the

TP region, which indirectly confirms the credibility of ML models for this precipitation estimation. The consistency of high CWP values with precipitation distribution further supports its critical role in this event, reinforcing the importance of cloud microphysical properties in precipitation estimation. To further assess the performance of our algorithm outside the training region, Fig. S5 includes a true-color satellite image of East Asia for this particular case and the estimation results. It can be observed that, although ML models were trained using ground observations from the China mainland, it still shows good consistency with GPM in terms of precipitation areas over the ocean. The precipitation areas in both the ML models and GPM correspond well to the distinct texture and bright cloud regions in the true-color satellite image. In terms of precipitation estimation, LightGBM shows a significant overestimation in areas surrounding some heavy precipitation centers compared to GPM, likely due to differences in meteorological conditions and cloud properties between land and ocean. In the future, it can be considered to continue the idea of this study by combining the transfer learning method to identify effective variables for quantitative precipitation estimation over the ocean, which is expected to further improve the performance of both ML algorithms and GPM in oceanic regions.

According to the aforementioned results, we find that the capabilities of precipitation retrieval for the XGBoost and LightGBM models are quite similar, but the LightGBM model has a much shorter training time. Therefore, we have determined LightGBM as the optimal model, and subsequent discussions will primarily focus on its results.

To obtain precipitation sensitivity factors for different climatic regions, the Shapley Additive Explanations (SHAP) approach is introduced. Fig. 7 shows the SHAP summary plot of LightGBM estimations in the humid and arid regions. The y-axis represents the importance of each feature in the estimation based on their Shapley values, and the top feature has the highest importance. The x-axis represents the SHAP values. Larger SHAP values indicate a greater impact on the estimation results. Positive SHAP values mean the feature increases the estimation values of precipitation, while negative values mean the feature decreases the estimation values of precipitation. The color indicates the value of the feature itself. Typically, a red dot means the feature value is high for that instance, and a blue dot means the feature value is low. Generally speaking, the SHAP analysis in Fig. 7 is largely consistent with feature importance in Table S3, with the spectral signals characterizing cloud properties and some meteorological variables (e.g. CAPE and K index) ranking high. For example, the cloud water path has the highest

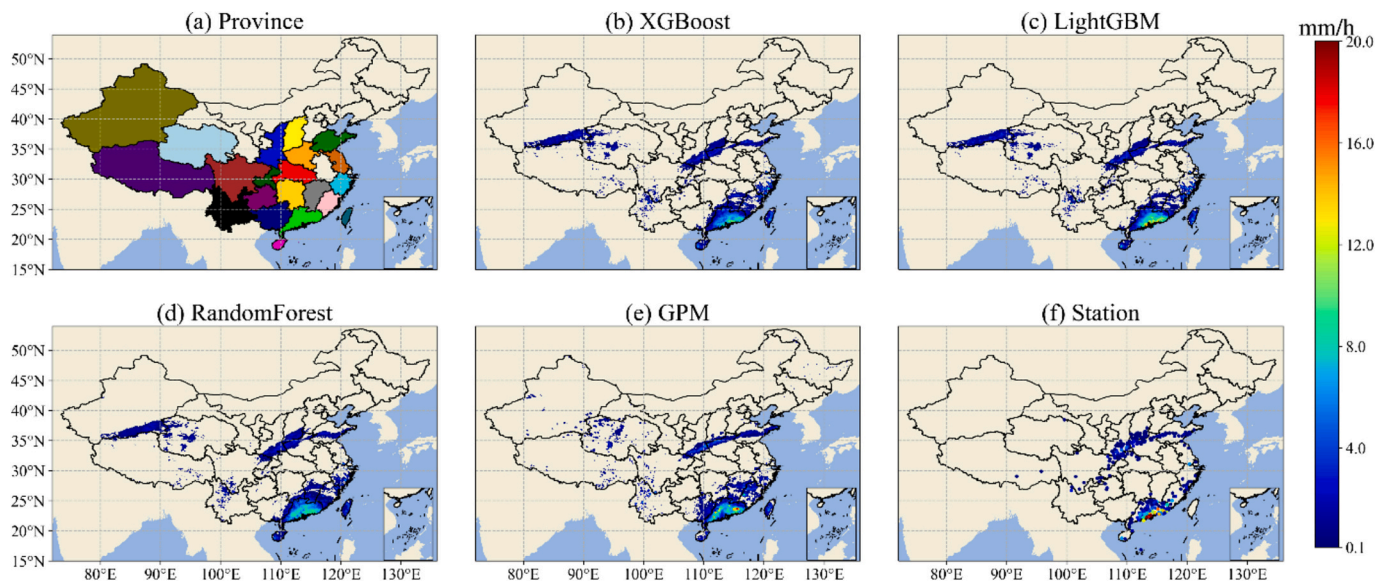


Fig. 6. Spatial distribution of precipitation for a case at 13:00 CST on 16 September 2018. (a) Affected provinces according to station observation. (b)–(f) Precipitation estimates from XGBoost, LightGBM, Random Forest, GPM-IMERG, and ground stations, respectively.

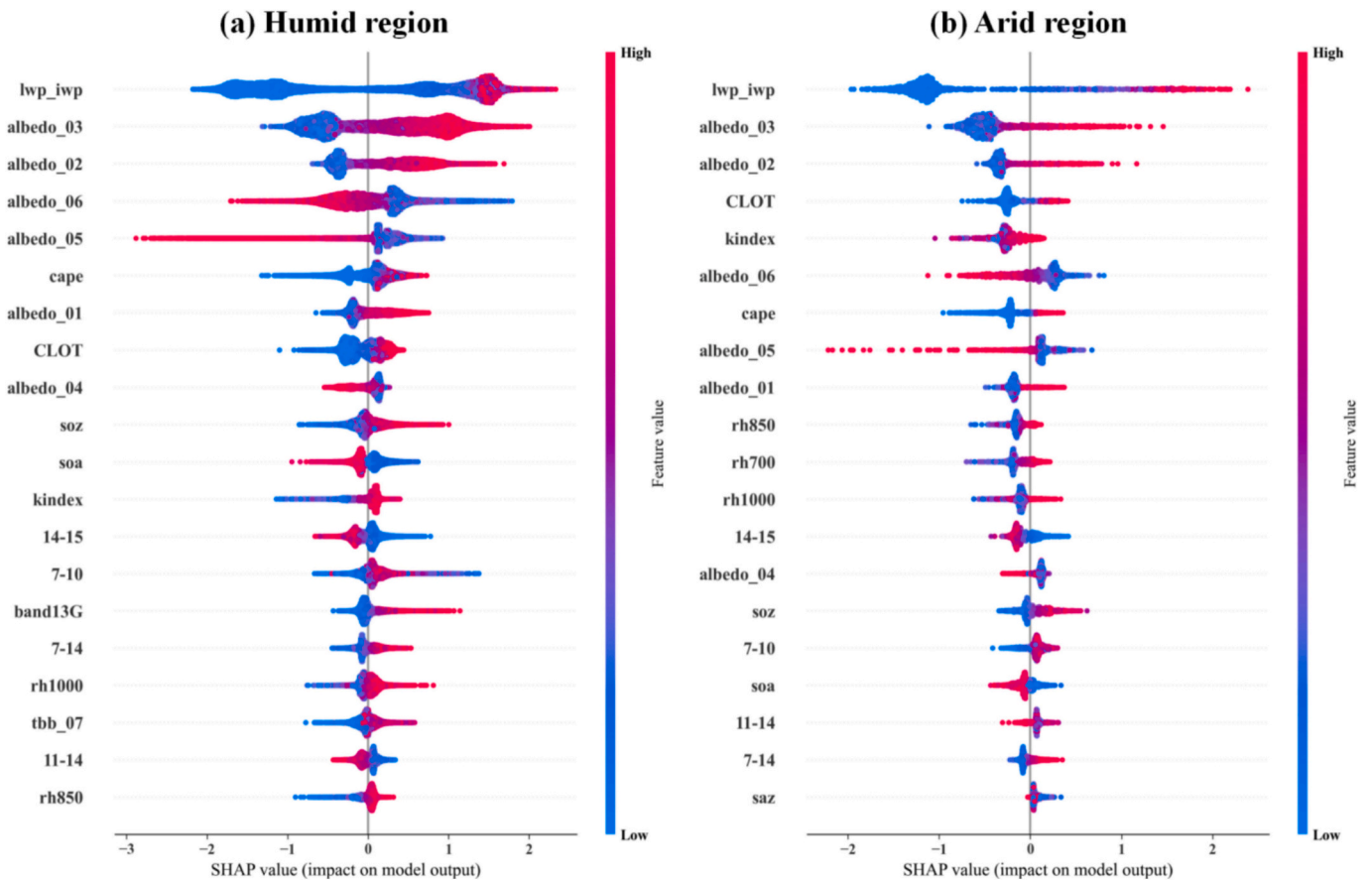


Fig. 7. The SHAP analysis of the LightGBM estimation for (a) Humid region, (b) Arid region. The position from top to bottom represents the ranking of feature importance. The color of the scatter represents the magnitude of feature values. A positive (negative) SHAP indicates positive (negative) contribution to the prediction. Only the top 20 variables ranked by SHAP feature importance are shown.

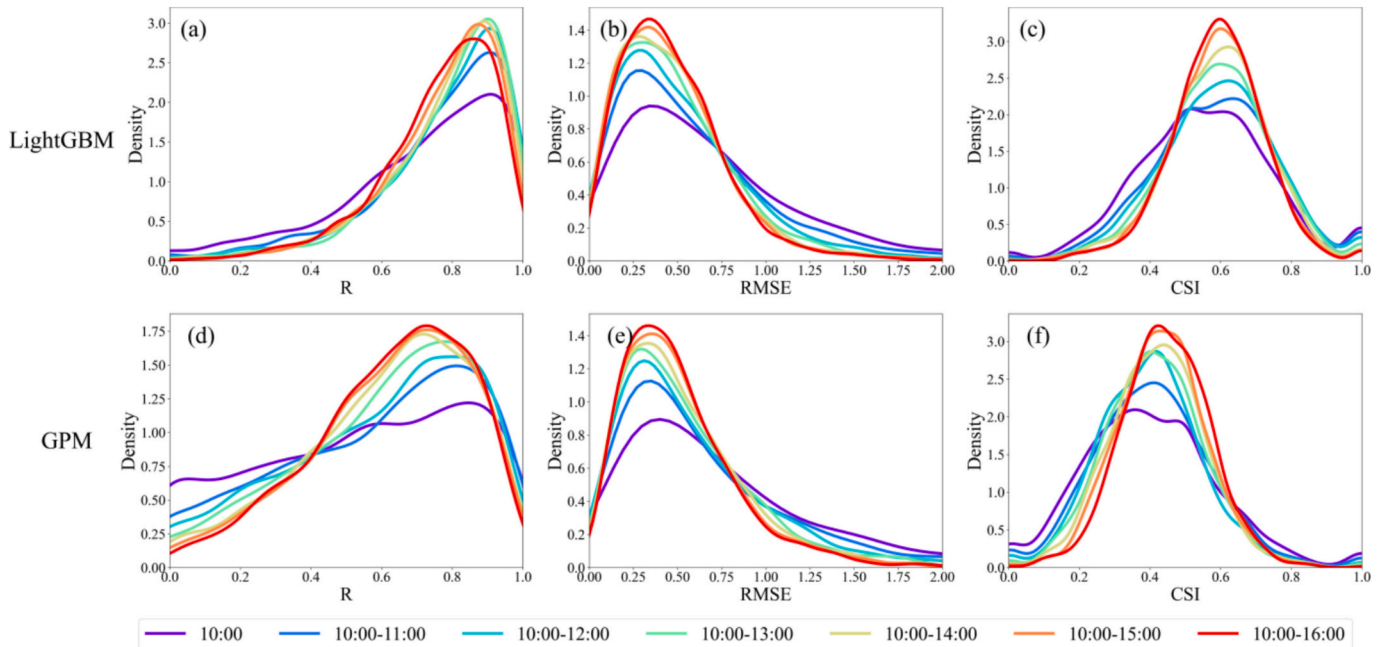


Fig. 8. Probability density function (PDF) curves of station evaluation metrics for LightGBM (a), (b), (c) and GPM (d), (e), (f). The color of the curves represents the average precipitation for the corresponding period.

importance for the LightGBM model, and its higher values are associated with higher precipitation estimation. However, there are still some differences between them, mainly due to differences in calculation method and information extraction. It is apparent from Fig. 7 and Fig. S6 that the relative humidity at different pressure levels (rh850, rh700 and rh1000) has greater importance as the environment becomes drier, probably because the evaporation of raindrops during falling process brings a higher influence for the model estimations (Salamalikis et al., 2016; Chen et al., 2020). In summary, the difference in the SHAP feature importance proves that the sensitivity factors for precipitation estimation are different across humid and arid regions, which will provide a valuable reference for the construction of regional QPE algorithms in the future.

In order to verify the temporal performance of our algorithm, Fig. 8 further depicts the probability density function (PDF) curves of evaluation metrics for cumulative hourly average precipitation from the LightGBM model and GPM product at all stations. Different curve colors represent the length of cumulative time. Generally, as the cumulative time increases, the PDF curve shape of all three metrics exhibits a transition from flat and wide to steep and narrow (see Figs. 8 (a)-(f)), which indicates that the metric values at all stations become more concentrated. Furthermore, the evaluation metrics corresponding to the peak probability density are also getting better. On one hand, this may be because both the LightGBM model and GPM product are capable of capturing the temporal pattern of rain rate. On the other hand, the estimation of single-hour rain rate is a highly nonlinear and complex problem with strong randomness and variability. After temporal averaging, some local noises are attenuated, so a better estimation can be obtained. However, when the cumulative time exceeds four hours (10:00–14:00), the peak of density and corresponding R for the LightGBM model slightly decline (see Fig. 8(a)), which is likely related to its poor performance in estimating convective precipitation that frequently occurs in the afternoon (Yu et al., 2014; Zheng et al., 2019). Additionally, the satellite VIS data is inevitably affected by solar zenith angle (SOZ). In the morning, the central and eastern regions generally experience relatively minor effect with a lower SOZ, while the western regions are significantly impacted. The situation is reversed in the afternoon. However, the density of ground observation stations in the eastern regions is significantly higher than that in the western regions, implying that the number of stations affected by SOZ increases gradually during the study period. Therefore, the utilization of VIS data as the training dataset for the LightGBM model with a high feature importance score is another reason for its slightly degradation of estimations. As for the GPM product, the peak of density gradually increases, but the corresponding R shows a significant decrease (see Fig. 8(d)). On one hand, the GPM product is mainly capable of capturing the diurnal cycle of convective precipitation, so the overall R values for all stations are increasing (Dai, 2024). On the other hand, as time accumulates, more samples with relatively poor estimations are introduced for averaging, which may lead to a decrease in the R values of stations with better estimations in the first few hours. The PDF curve shapes of RMSE and CSI for GPM and LightGBM are similar, but the LightGBM estimations tend to concentrate around a superior CSI value (Figs. 8(c) and (f)).

Tian et al. (2009) noted that a thorough investigation of the sources of errors in precipitation products will help identify key aspects for algorithm improvement and enhance their application for users. Therefore, the total absolute error of estimated rain rate (E_t) is decomposed into hit error E_h , false error E_f , and missed error E_m :

$$E_t = \sum |P_{obs} - P_{est}| \quad (12)$$

$$E_h = \sum |P_{obs}^h - P_{est}^h| \quad (13)$$

$$E_f = \sum |P_{obs}^f - P_{est}^f| \quad (P_{obs}^f = 0) \quad (14)$$

$$E_m = \sum |P_{obs}^m - P_{est}^m| \quad (P_{est}^m = 0) \quad (15)$$

$$E_t = E_h + E_f + E_m \quad (16)$$

where E_t , E_h , E_f and E_m denote total, hit, false and missed error (unit: mm), respectively; P_{obs} represents rain rate from gauge observations; P_{est} represents rain rate from algorithm or product estimations; h , f and m denote hit, false and missed events, respectively. Table 3 lists the mean absolute hit error, false error and missed error (MAE_h , MAE_f and MAE_m) for the LightGBM model and GPM product, which is computed by dividing E_h , E_f and E_m by the number of hit, false and missed events, respectively. The percentages of these error components relative to E_t (e_h , e_m and e_f) are also provided in parentheses. It can be clearly seen that the LightGBM model has lower MAE_h , MAE_m and MAE_f compared to the GPM product, suggesting that it has advantages in both precipitation identification and estimation. Notably, the LightGBM model rarely misses precipitation events, with a MAE_m of only 0.443 mm (e_m accounts only for 3%), as shown in Table 3. The MAE_h and e_h are the highest in both LightGBM and GPM, indicating that they still need improvement in the aspect of accurate rain rate retrieval. In order to further compare the error components of the LightGBM model and GPM product at different moments, Fig. 9 shows their temporal variation of MAE_h , MAE_f and MAE_m . Before 12:00, MAE_h , MAE_f and MAE_m of the LightGBM model are relatively small, indicating that it performs well in retrieving stratiform precipitation, which frequently occurs during this period. In the afternoon, convective precipitation becomes dominant, and both LightGBM and GPM have high values for three error components, which indicates that their estimations for convective precipitation still need to be improved. It is worth noting that the MAE_f of the GPM product is reduced in the retrieval of frequently occurred convective precipitation compared to LightGBM after 14:00 (Fig. 9(b)), which may be related to its capability to penetrate cloud and resolve some information about cloud vertical structure.

4.4. Analysis by Cloud Type

In the real atmosphere, different types of clouds are dominated by different physical processes, and has dramatically distinct precipitation characteristics (Yan and Liu, 2019; Afzali Goroooh et al., 2020). Here, we adopted the research method similar to that used by Zhao et al. (2022), which classifying cloud precipitation samples to different cloud types based on the joint distribution of cloud top pressure and optical thickness, as shown in Fig. 10. In general, with the decrease of cloud top pressure and the increase of cloud optical thickness, the rain rate should significantly increase. This is because the deeper and more vigorous the cloud develops, the easier it is to generate heavy precipitation. It can be seen from Figs. 10 (c) and (f) that a large proportion of the samples of thin clouds (cloud optical thickness is very small) or cirrus clouds (cloud top pressure is very low) have CSI values that are not equal to 0, which means that they also correspond to the occurrence of surface precipitation. We think that this may be because the tops of deep convective clouds are often covered with ice phase anvil clouds, and raindrops may experience displacement during descent within the convective system

Table 3

The mean absolute hit error, false error and missed error (MAE_h , MAE_f and MAE_m) for LightGBM and GPM-IMERG in the independent validation dataset. The percentages of hit error, missed error and false error to total absolute error (e_h , e_m , e_f and e_t) are shown in parentheses.

Name	MAE_h ($e_h = E_h/E_t$)	MAE_m ($e_m = E_m/E_t$)	MAE_f ($e_f = E_f/E_t$)	MAE_t ($e_t = E_t/E_t$)
LightGBM	2.199 (70 %)	0.443 (3 %)	1.023 (27 %)	0.214 (100 %)
GPM	2.463 (54 %)	1.146 (17 %)	1.112 (29 %)	0.225 (100 %)

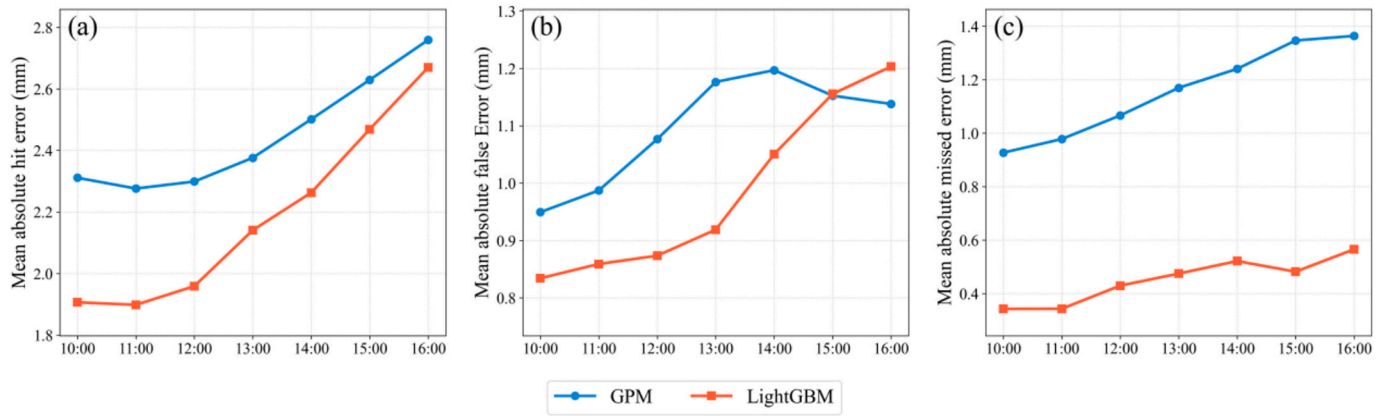


Fig. 9. Variation of mean absolute error components from 10:00 to 16:00 for LightGBM and GPM-IMERG. (a) Mean absolute hit error (MAE_h), (b) Mean absolute false error (MAE_f), and (c) Mean absolute missed error (MAE_m).

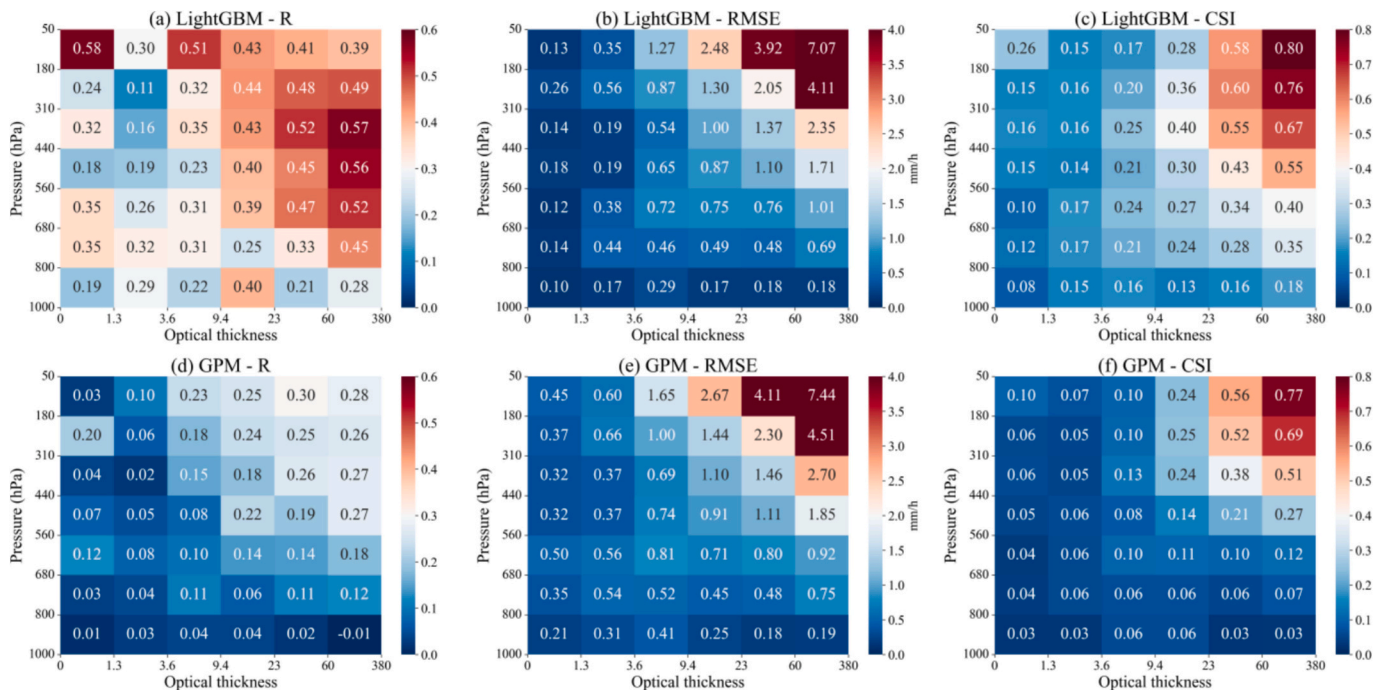


Fig. 10. Evaluation metrics R, RMSE and CSI joint histogram of cloud top pressure (PC) and cloud optical thickness (τ) for LightGBM and GPM-IMERG based on the independent validation dataset. It should be noted that the color of the numbers has no special meaning.

due to strong horizontal wind shear, resulting in a mismatch between the actual surface observations and the anvil clouds above (Dai et al., 2013). In Figs. 10(a) and (d), it is evident that the R values of the LightGBM model is slightly higher than that of GPM, particularly for samples with high cloud optical thickness but not very low cloud top pressure. The cloud in these samples is usually underdeveloped and produces moderate precipitation rate that can be well estimated by LightGBM. When the cloud top pressure drops below 310 hPa, the R values of LightGBM start to decrease (Fig. 10(a)). This may be because the cloud is fully developed at this point, and the passive satellite spectral signals cannot penetrate such clouds and may suffer from signal saturation issues, therefore leading to poor estimation (Ba and Gruber, 2001; Lazri and Ameur, 2016). In contrast, due to the strong penetration ability of microwave observation signals to resolve information about cloud vertical structure, the GPM product shows relatively consistent performance in estimating rain rate from fully developed cloud compared to less developed cloud (Fig. 10(d)). In terms of RMSE and CSI (Figs. 10 (b), (e), (c) and (f)), the differences from the LightGBM model

and GPM product are quite small for typical samples with larger cloud optical thickness and lower cloud top pressure. However, for some less developed thin or cirrus cloud samples (low cloud optical depth or high cloud top pressure), these two evaluation metrics from the GPM product are slightly worse than those from LightGBM. On one hand, the GPM has a limited ability to detect these fine and light precipitation events (Li et al., 2021a, 2021b). On the other hand, the coarser spatial resolution of GPM makes it easier to misjudge non-precipitation pixels around the precipitation center as precipitation pixels. These may also be major causes of its high FAR value. The cloud type analysis is also applied to the case in Fig. 6 and the result is similar.

5. Conclusions

The retrieval of high-precision precipitation dataset is essential for physical process analysis of precipitation event, meteorological forecast model improvement and disaster warning deployment. Due to the complex and diverse physical processes involved in precipitation, it

remains unclear which variables are effective for satellite-based quantitative precipitation estimation. Traditional retrieval methods often struggle to construct non-linear relationship between predictor variables and rain rate, and some important cloud parameters, meteorological field information are often overlooked. In this study, we used machine learning methods to enhance precipitation retrieval accuracy by incorporating more effective information. We further conducted an in-depth analysis focusing on four aspects: the importance of input variables on precipitation estimations, spatial and temporal evaluation and regional sensitivity factor, comparison with other dataset, and algorithm performance for different cloud types. The main conclusions are summarized as follows:

- (1) We discussed the importance and the degree of information gain of input variables in machine learning models through multiple sensitivity tests. The results indicate that each variable used in this study is beneficial to the algorithm estimations. The overall ranking of the variables in terms of their feature importance score is as follows: satellite VIS channel, cloud property, satellite IR channel, and meteorological background field. Cloud water path from cloud property product ranks the highest. The information provided by some IR brightness channels and meteorological variables (e.g., temperature at different pressure levels) is relatively limited.
- (2) To mitigate the effect of highly-skewed and heavy-tailed distributions of hourly precipitation on machine learning predictions, some preprocessing techniques, such as sample balancing, and logarithmic processing were adopted. In this study, we used three machine learning models including Random Forest, XGBoost and LightGBM. The results show that when considering both precipitation estimation performance and computational runtime, the LightGBM is the best model, which can effectively capture temporal variation features and accurately reflect spatial distributions. For all regions, cloud parameters (e.g., cloud water path) are the most effective factors for precipitation estimation. However, when the environment becomes drier, information of relative humidity at different pressure levels becomes increasingly important.
- (3) The rain rate derived from GPM IMERG Final-Run v07 was compared with Machine Learning estimations. Overall, the quantitative precipitation estimation from the LightGBM model is comparable to GPM product, and even outperforms GPM in some cases. This further validates the effectiveness of our variable selection. The LightGBM model significantly improves the conditions where precipitation is actually present but not identified by GPM. The results of the error decomposition show that both LightGBM and GPM need to improve their performance in the aspect of accurate rain rate retrieval, especially for convective precipitation.
- (4) The capability of the LightGBM model to capture precipitation characteristics for different types of clouds was further investigated. It is apparent that both LightGBM and GPM exhibit precipitation estimation performance that is highly dependent on cloud types. The LightGBM model has the best estimation for samples with high cloud optical thickness but not very low cloud top pressure, due to its better capability in the retrieval of moderate rain rate. For samples with fully developed clouds, the LightGBM model shows a relatively poor performance, which may be attributed to the fact that the passive satellite spectral signals cannot penetrate deep convective cloud and may suffer from signal saturation issues in this situation.

Previous studies have focused on using only the IR channel considering the all-weather applicability of the retrieval algorithm. However, our results show that the VIS channel is valuable for the improvement of precipitation estimation accuracy, which may be related to the fact that

the VIS channel contains some key information about cloud characteristics, such as cloud water. Although the machine learning method we used has achieved better performance compared to GPM, this may be due to our incorporation of more variables. Additionally, the algorithm was trained using ground observations as true values, which may unfairly highlight the advantages of the machine learning algorithm due to GPM does not use training to acquire the characteristics of ground observations. Therefore, combining the effective variables into GPM's retrieval or merging algorithms, and utilizing machine learning methods to establish nonlinear relationships between GPM and ground observations, may further enhance its performance. Furthermore, GPM is a global precipitation product with broad application scenarios, but the performance of the present ML algorithm outside of mainland China still requires further validation. In the future, continuing the approach of this study and incorporating transfer learning methods to identify effective variables for quantitative precipitation estimation across different regions globally, as well as enhancing the performance of ML algorithms, will be our advantage. In this study, we want to emphasize that the goal of this study is not to develop an innovative satellite-based quantitative precipitation estimation algorithm but to focus on identifying which variables are most effective in improving the accuracy of satellite precipitation retrievals. This research aims to provide valuable insights for the selection of variables in the fusion and retrieval processes of advanced precipitation products like GPM in future updates. Additionally, it seeks to offer recommendations for improving climate models, satellite precipitation retrievals, and precipitation forecasting across different scenarios, such as varying cloud types and meteorological conditions.

In summary, this study still has some uncertainties and significant room for improvement. Firstly, existing ground-based precipitation observations are very limited in this study, especially in the northwestern regions of the China mainland, posing significant challenges for the application of machine learning in these areas. Secondly, as the key information for satellite precipitation retrieval, the quality of cloud property products also introduces great uncertainty in quantitative precipitation estimation, whereas more accurate and long-time series cloud property products can provide stronger data support for algorithm construction and effective variables verification (Li et al., 2013a; Wang et al., 2022a; Zhuge et al., 2024). Thirdly, the VIS/IR sensors of passive satellites are only limited to the observation of cloud tops, but cloud has a three-dimensional structural feature (Li et al., 2018b; Li et al., 2019; Teng et al., 2020; Zhao et al., 2023; Zhao et al., 2024b). The presence of multi-layer clouds significantly affects the retrieval accuracy of cloud properties from passive satellite observations, and the vertical structure information within cloud usually implies the complex physical processes of cloud and raindrop particles, which are closely related to the occurrence and evolution of precipitation (Luo et al., 2014; Li et al., 2018a; Kikuchi and Suzuki, 2019; Teng et al., 2023). Therefore, attempting to integrate the advantages of both passive and active satellites, utilizing machine learning or deep learning methods, taking the passive satellite VIS/IR channels as inputs, and the cloud vertical structure detected by active satellite as ground truth, developing a cloud vertical structure retrieval algorithm, and obtaining cloud vertical structure information and further verify its importance could be an excellent enhancement strategy. Furthermore, hazardous storm events are typically characterized by rapid evolution, heavy precipitation intensity and short duration, so it is of practical significance to reduce the time interval of satellite observations and improve the temporal resolution of precipitation products. Finally, machine learning methods integrated with physical constraints can help us better understand the complex physical mechanisms of precipitation, which may be one of the hot issues for future research.

CRediT authorship contribution statement

Sihang Xu: Writing – original draft, Visualization, Software,

Methodology, Investigation, Data curation. **Jiming Li**: Writing – review & editing, Visualization, Validation, Supervision, Project administration, Methodology, Conceptualization. **Jia Li**: Visualization, Software, Data curation. **Deyu Wen**: Investigation, Data curation. **Miao Lei**: Software, Data curation. **Yuan Wang**: Writing – review & editing, Supervision. **Jianping Huang**: Writing – review & editing, Supervision.

Declaration of competing interest

The authors declare that they have no known competing financial interests or personal relationships that could have appeared to influence the work reported in this paper.

Acknowledgments

This research was jointly supported by the key Program of the National Natural Science Foundation of China (42430601), the Major Program of the National Natural Science Foundation of China (42090030) and the National Science Fund for Excellent Young Scholars (42022037). The authors declare that they have no conflicts of interest. We would like to thank the Himawari-8, ERA5, NASA, NOAA - CMORPH Climate Data Record (CDR), GloH2O's MSWEP, National Tibetan Plateau / Third Pole Environment Data Center TPHiPr and CMA science teams for providing excellent and accessible data products that made this study possible.

Appendix A. The meaning of the evaluation metrics

Among all the classification evaluation metrics, probability of detection (POD) represents the proportion of actual precipitation events that are correctly identified and false alarm ratio (FAR) indicates the fraction of identified precipitation events that did not actually occur. Critical success index (CSI) can be understood as a metric that comprehensively considers both POD and FAR. Accuracy rate (ACC) represents the probability of a sample is correctly classified. Heidke skill score (HSS) and equitable threat score (ETS) both indicate the degree of improvement of the algorithm compared to random predictions. Except for FAR, the optimal values for all the above-mentioned metrics are 1, and the optimal value for FAR is 0. Regression evaluation metrics Pearson correlation coefficient (R), mean absolute error (MAE), and root mean square error (RMSE) indicate the consistency between the algorithm estimations and the observations, where a higher R value is better, and lower values for MAE and RMSE are preferred.

Appendix B. Supplementary data

Supplementary data to this article can be found online at <https://doi.org/10.1016/j.atmosres.2025.108112>.

Data availability

The Himawari-8 level-1 product is publicly available through the JAXA P-Tree System at <https://www.eorc.jaxa.jp/ptree/>. The ground rain gauge data are available from the website of the China Meteorological Administration: <http://data.cma.cn>. The GPM IMERG Final-Run V07 used in this study is available from the following websites: <https://gpm.nasa.gov/data/directory>. The ERA5 hourly data on single levels and pressure levels are available from Climate Data Store (CDS) of <https://cds.climate.copernicus.eu/cdsapp#!/search?text=ERA5>. The Satellite Cloud and Radiation Property retrieval System (SatCORPS) Clouds and the Earth's Radiant Energy System (CERES) Geostationary Satellite (GEO) Edition 4 Himawari-8 over the Northern Hemisphere (NH) Version 1.2 data product is available from the following website: https://asdc.larc.nasa.gov/data/CERES/GEO/Edition4/HIM08_NH_V01.2/.

References

- Adler, R.F., Negri, A.J., 1988. A Satellite infrared Technique to Estimate Tropical Convective and Stratiform Rainfall. *J. Appl. Meteorol. Climatol.* 27 (1), 30–51. [https://doi.org/10.1175/1520-0450\(1988\)027<0030:ASITTE>2.0.CO;2](https://doi.org/10.1175/1520-0450(1988)027<0030:ASITTE>2.0.CO;2).
- Afzali Goroo, V., et al., 2020. Deep Neural Network Cloud-Type Classification (DeepCTC) Model and its Application in evaluating PERSIANN-CCS. *Remote Sens.* <https://doi.org/10.3390/rs12020316>.
- Akbari Asanjan, A., et al., 2018. Short-Term Precipitation Forecast based on the PERSIANN System and LSTM Recurrent Neural Networks. *J. Geophys. Res. Atmos.* 123 (22), 12,543–12,563. <https://doi.org/10.1029/2018JD028375>.
- Ba, M.B., Gruber, A., 2001. GOES Multispectral Rainfall Algorithm (GMSRA). *J. Appl. Meteorol.* 40 (8), 1500–1514. [https://doi.org/10.1175/1520-0450\(2001\)040<1500:GMRAG>2.0.CO;2](https://doi.org/10.1175/1520-0450(2001)040<1500:GMRAG>2.0.CO;2).
- Baum, B.A., et al., 2000. Remote sensing of cloud properties using MODIS airborne simulator imagery during SUCCESS: 1. Data and models. *J. Geophys. Res.-Atmos.* 105 (D9), 11767–11780. <https://doi.org/10.1029/1999JD901089>.
- Beck, H.E., et al., 2019. MSWEP V2 Global 3-Hourly 0.1° Precipitation: Methodology and Quantitative Assessment. *Bull. Am. Meteorol. Soc.* 100, 473–500. <https://doi.org/10.1175/BAMS-D-17-0138.1>.
- Bedka, K., et al., 2010. Objective Satellite-based Detection of Overshooting Tops using infrared Window Channel Brightness Temperature Gradients. *J. Appl. Meteorol. Climatol.* 49 (2), 181–202. <https://doi.org/10.1175/2009JAMC2286.1>.
- Behrang, A., Hsu, K., Imam, B., Sorooshian, S., Huffman, G.J., Kuligowski, R.J., 2009. PERSIANN-MSA: a precipitation estimation method from satellite-based multispectral analysis. *J. Hydrometeorol.* 10, 1414–1429. <https://doi.org/10.1175/2009JHM1139.1>.
- Bony, S., et al., 2013. Robust direct effect of carbon dioxide on tropical circulation and regional precipitation. *Nat. Geosci.* 6 (6), 447–451. <https://doi.org/10.1038/ngeo1799>.
- Breiman, L., 2001. Random Forests. *Mach. Learn.* 45 (1), 5–32. <https://doi.org/10.1023/A:1010933404324>.
- Brown, R.G., Zhang, C., 1997. Variability of midtropospheric moisture and its effect on cloud-top height distribution during TOGA COARE. *J. Atmos. Sci.* 54, 2760–2774. [https://doi.org/10.1175/1520-0469\(1997\)054<2760:VOMMAI>2.0.CO;2](https://doi.org/10.1175/1520-0469(1997)054<2760:VOMMAI>2.0.CO;2).
- Chang, F.-L., Li, Z., 2002. Estimating the vertical variation of cloud droplet effective radius using multispectral near-infrared satellite measurements. *J. Geophys. Res. Atmos.* 107 (D15). <https://doi.org/10.1029/2001JD000766>. AAC 7-1-AAC 7-12.
- Chen, T., Guestrin, C., 2016. XGBoost: A Scalable Tree Boosting System, Proceedings of the 22nd ACM SIGKDD International Conference on Knowledge Discovery and Data Mining. Association for Computing Machinery, San Francisco, California, USA, pp. 785–794. <https://doi.org/10.1145/2939672.2939785>.
- Chen, T.-C., Pfaendner, J., 1993. On the Atmospheric Branch of the Hydrological Cycle. *J. Clim.* 6 (1), 161–167.
- Chen, H., Chen, Y., Li, D., Li, W., 2020. Effect of sub-cloud evaporation on precipitation in the Tianshan Mountains (Central Asia) under the influence of global warming. *Hydrol. Process.* 34 (26), 5557–5566. <https://doi.org/10.1002/hyp.13969>.
- Chen, S., et al., 2022a. A high-resolution monitoring approach of canopy urban heat island using a random forest model and multi-platform observations. *Atmos. Meas. Tech.* 15 (3), 735–756. <https://doi.org/10.5194/amt-15-735-2022>.
- Chen, Y., Huang, J., Song, X., Wen, H., Song, H., 2022b. Evaluation of the Impacts of rain Gauge Density and distribution on Gauge-Satellite Merged Precipitation estimates. *IEEE Trans. Geosci. Remote Sens.* 60, 1–18. <https://doi.org/10.1109/TGRS.2020.3037099>.
- Chiu, J.C., Holmes, J.A., Hogan, R.J., O'Connor, E.J., 2014. The interdependence of continental warm cloud properties derived from unexploited solar background signals in ground-based lidar measurements. *Atmos. Chem. Phys.* 14 (16), 8389–8401. <https://doi.org/10.5194/acp-14-8389-2014>.
- Dabberdt, W.F., Schlatter, T.W., 1996. Research Opportunities from Emerging Atmospheric observing and Modeling Capabilities. *Bull. Am. Meteorol. Soc.* 77 (2), 305–324. [https://doi.org/10.1175/1520-0477\(1996\)077<0305:ROFEAO>2.0.CO;2](https://doi.org/10.1175/1520-0477(1996)077<0305:ROFEAO>2.0.CO;2).
- Dai, A., 2024. The diurnal cycle from observations and ERA5 in precipitation, clouds, boundary layer height, buoyancy, and surface fluxes. *Clim. Dyn.* <https://doi.org/10.1007/s00382-024-07182-6>.
- Dai, Q., Han, D., Rico-Ramirez, M.A., Islam, T., 2013. The impact of raindrop drift in a three-dimensional wind field on a radar-gauge rainfall comparison. *Int. J. Remote Sens.* 34 (21), 7739–7760. <https://doi.org/10.1080/01431161.2013.826838>.
- Duncan, J.M.A., Biggs, E.M., Dash, J., Atkinson, P.M., 2013. Spatio-temporal trends in precipitation and their implications for water resources management in climate sensitive Nepal. *Appl. Geogr.* 43, 138–146. <https://doi.org/10.1016/j.apgeog.2013.06.011>.
- Ebert, E.E., Janowiak, J.E., Kidd, C., 2007. Comparison of Near-Real-Time Precipitation estimates from Satellite Observations and Numerical Models. *Bull. Am. Meteorol. Soc.* 88 (1), 47–64. <https://doi.org/10.1175/BAMS-88-1-47>.
- Feng, S., Fu, Q., 2013. Expansion of global drylands under a warming climate. *Atmos. Chem. Phys.* 13 (19), 10081–10094. <https://doi.org/10.5194/acp-13-10081-2013>.
- Gautam, A.K., Pandey, A., 2022. Ground validation of GPM Day-1 IMERG and TMPA Version-7 products over different rainfall regimes in India. *Theor. Appl. Climatol.* 149 (3), 931–943. <https://doi.org/10.1007/s00704-022-04091-8>.
- Gavahi, K., Foroumandi, E., Moradkhani, H., 2023. A deep learning-based framework for multi-source precipitation fusion. *Remote Sens. Environ.* 295, 113723. <https://doi.org/10.1016/j.rse.2023.113723>.
- Hong, Y., Hsu, K.-L., Sorooshian, S., Gao, X., 2004. Precipitation Estimation from Remotely Sensed Imagery using an Artificial Neural Network Cloud Classification

- System. *J. Appl. Meteorol.* 43 (12), 1834–1853. <https://doi.org/10.1175/JAM2173.1>.
- Hong, Y., Hsu, K.-L., Sorooshian, S., Gao, X., 2005. Self-organizing nonlinear output (SONO): a neural network suitable for cloud patch-based rainfall estimation at small scales. *Water Resour. Res.* 41 (3). <https://doi.org/10.1029/2004WR003142>.
- Horváth, A., Davies, R., 2007. Comparison of microwave and optical cloud water path estimates from TMI, MODIS, and MISR. *J. Geophys. Res. Atmos.* 112 (D1). <https://doi.org/10.1029/2006JD007101>.
- Hou, A.Y., et al., 2014. The Global Precipitation Measurement Mission. *Bull. Am. Meteorol. Soc.* 95 (5), 701–722. <https://doi.org/10.1175/BAMS-D-13-00164.1>.
- Huang, J., Yu, H., Guan, X., Wang, G., Guo, R., 2016. Accelerated dryland expansion under climate change. *Nat. Clim. Chang.* 6 (2), 166–171. <https://doi.org/10.1038/nclimate2837>.
- Huffman, G.J., et al., 1997. The Global Precipitation Climatology Project (GPCP) combined Precipitation Dataset. *Bull. Am. Meteorol. Soc.* 78 (1), 5–20. [https://doi.org/10.1175/1520-0477\(1997\)078<0005:GPCPG>2.0.CO;2](https://doi.org/10.1175/1520-0477(1997)078<0005:GPCPG>2.0.CO;2).
- Huffman, G.J., et al., 2007. The TRMM Multisatellite Precipitation Analysis (TMPA): Quasi-Global, Multiyear, Combined-Sensor Precipitation estimates at Fine Scales. *J. Hydrometeorol.* 8 (1), 38–55. <https://doi.org/10.1175/JHM560.1>.
- Jian, B., et al., 2022. Competition between Radiative and Seeding Effects of Overlying Clouds on underlying Marine Stratocumulus. *Geophys. Res. Lett.* 49 (23), e2022GL100729. <https://doi.org/10.1029/2022GL100729>.
- Jiang, Y., et al., 2023. TPHiPr: a long-term (1979–2020) high-accuracy precipitation dataset (1/30°, daily) for the Third Pole region based on high-resolution atmospheric modeling and dense observations. *Earth Syst. Sci. Data* 15 (2), 621–638. <https://doi.org/10.5194/essd-15-621-2023>.
- Jin, H., Chen, X., Wu, P., Song, C., Xia, W., 2021. Evaluation of spatial-temporal distribution of precipitation in mainland China by statistic and clustering methods. *Atmos. Res.* 262, 105772. <https://doi.org/10.1016/j.atmosres.2021.105772>.
- Joyce, R.J., Janowiak, J.E., Arkin, P.A., Xie, P., 2004. CMORPH: A Method that Produces Global Precipitation estimates from Passive Microwave and infrared Data at High Spatial and Temporal Resolution. *J. Hydrometeorol.* 5 (3), 487–503. [https://doi.org/10.1175/1525-7541\(2004\)005<0487:CAMTPG>2.0.CO;2](https://doi.org/10.1175/1525-7541(2004)005<0487:CAMTPG>2.0.CO;2).
- Ke, G., et al., 2017. LightGBM: A Highly Efficient Gradient Boosting Decision Tree, Proceedings of the 31st International Conference on Neural Information Processing Systems. Curran Associates Inc., Long Beach, California, USA, pp. 3149–3157.
- Kidd, C., et al., 2016. Global Precipitation estimates from Cross-Track Passive Microwave Observations using a Physically based Retrieval Scheme. *J. Hydrometeorol.* 17 (1), 383–400. <https://doi.org/10.1175/JHM-D-15-0051.1>.
- Kikuchi, M., Suzuki, K., 2019. Characterizing Vertical Particle Structure of Precipitating Cloud System from Multiplatform Measurements of A-Train Constellation. *Geophys. Res. Lett.* 46 (2), 1040–1048. <https://doi.org/10.1029/2018GL081244>.
- Koch, E., Naveau, P., 2015. A frailty-contagion model for multi-site hourly precipitation driven by atmospheric covariates. *Adv. Water Resour.* 78, 145–154. <https://doi.org/10.1016/j.advwatres.2015.01.001>.
- Kühnlein, M., Thies, B., Nauss, T., Bendix, J., 2010. Rainfall-Rate Assignment Using MSG SEVIRI Data—A Promising Approach to Spaceborne Rainfall-Rate Retrieval for Midlatitudes. *J. Appl. Meteorol. Climatol. - J. APPL. METEOROL. CLIMATOL.* 49, 1477–1495. <https://doi.org/10.1175/2010JAMC2284.1>.
- Lazri, M., Ameer, S., 2016. Using cloud water path and cloud top temperature for estimating convective and stratiform rainfall from SEVIRI daytime data. *Arab. J. Geosci.* 9 (11), 577. <https://doi.org/10.1007/s12517-016-2610-8>.
- Lei, M., et al., 2022. Inconsistent Frequency Trends between Hourly and Daily Precipitation during warm season in mainland of China. *Geophys. Res. Lett.* 49 (19), e2022GL100277. <https://doi.org/10.1029/2022GL100277>.
- Lenderink, G., van Meijgaard, E., 2008. Increase in hourly precipitation extremes beyond expectations from temperature changes. *Nat. Geosci.* 1 (8), 511–514. <https://doi.org/10.1038/ngeo262>.
- Lensky, I.M., Rosenfeld, D., 2003. Satellite-based Insights into Precipitation Formation Processes in Continental and Maritime Convective Clouds at Nighttime. *J. Appl. Meteorol.* 42 (9), 1227–1233. [https://doi.org/10.1175/1520-0450\(2003\)042<1227:SIIPFP>2.0.CO;2](https://doi.org/10.1175/1520-0450(2003)042<1227:SIIPFP>2.0.CO;2).
- Letu, H., et al., 2019. Ice Cloud Properties from Himawari-8/AHI Next-Generation Geostationary Satellite: Capability of the AHI to Monitor the DC Cloud Generation Process. *IEEE Trans. Geosci. Remote Sens.* 57 (6), 3229–3239. <https://doi.org/10.1109/TGRS.2018.2882803>.
- Letu, H., et al., 2020. High-resolution retrieval of cloud microphysical properties and surface solar radiation using Himawari-8/AHI next-generation geostationary satellite. *Remote Sens. Environ.* 239, 111583. <https://doi.org/10.1016/j.rse.2019.111583>.
- Letu, H., et al., 2023. Surface Solar Radiation Compositions Observed from Himawari-8/9 and Fengyun-4 Series. *Bull. Am. Meteorol. Soc.* 104 (10), E1772–E1789. <https://doi.org/10.1175/BAMS-D-22-0154.1>.
- Li, J.M., et al., 2013a. A new approach to retrieve cloud base height of marine boundary layer clouds. *Geophys. Res. Lett.* 40 (16), 4448–4453. <https://doi.org/10.1002/grl.50836>.
- Li, Z., Yang, D., Hong, Y., 2013b. Multi-scale evaluation of high-resolution multi-sensor blended global precipitation products over the Yangtze River. *J. Hydrol.* 500, 157–169. <https://doi.org/10.1016/j.jhydrol.2013.07.023>.
- Li, J., et al., 2018a. Long-term variation of cloud droplet number concentrations from space-based Lidar. *Remote Sens. Environ.* 213, 144–161. <https://doi.org/10.1016/j.rse.2018.05.011>.
- Li, J., et al., 2018b. The impact of atmospheric stability and wind shear on vertical cloud overlap over the Tibetan Plateau. *Atmos. Chem. Phys.* 18 (10), 7329–7343. <https://doi.org/10.5194/acp-18-7329-2018>.
- Li, J., et al., 2019. Atmospheric Instability Dominates the Long-Term Variation of Cloud Vertical Overlap over the Southern Great Plains Site. *J. Geophys. Res. Atmos.* 124 (16), 9691–9701. <https://doi.org/10.1029/2019JD030954>.
- Li, X., et al., 2021a. Leveraging machine learning for quantitative precipitation estimation from Fengyun-4 geostationary observations and ground meteorological measurements. *Atmos. Meas. Tech.* 14 (11), 7007–7023. <https://doi.org/10.5194/amt-14-7007-2021>.
- Li, X., Sungmin, O., Wang, N., Liu, L., Huang, Y., 2021b. Evaluation of the GPM IMERG V06 products for light rain over mainland China. *Atmos. Res.* 253, 105510. <https://doi.org/10.1016/j.atmosres.2021.105510>.
- Li, D., et al., 2022. Response of Cloud and Precipitation Properties to Seeding at a Supercooled Cloud-Top Layer. *Earth and Space Science* 9 (9), e2021EA001791. <https://doi.org/10.1029/2021EA001791>.
- Lin, H., et al., 2022. Estimate of daytime single-layer cloud base height from advanced baseline imager measurements. *Remote Sens. Environ.* 274, 112970. <https://doi.org/10.1016/j.rse.2022.112970>.
- Long, K., et al., 2021. Higher Temperature Enhances Spatiotemporal Concentration of Rainfall. *J. Hydrometeorol.* 22 (12), 3159–3169. <https://doi.org/10.1175/JHM-D-21-0034.1>.
- Luo, Z.J., Jeyaratnam, J., Iwasaki, S., Takahashi, H., Anderson, R., 2014. Convective vertical velocity and cloud internal vertical structure: an A-Train perspective. *Geophys. Res. Lett.* 41 (2), 723–729. <https://doi.org/10.1002/2013GL058922>.
- Ma, Z., et al., 2020. An updated moving window algorithm for hourly-scale satellite precipitation downscaling: a case study in the Southeast Coast of China. *J. Hydrol.* 581, 124378. <https://doi.org/10.1016/j.jhydrol.2019.124378>.
- Ma, Z., Zhu, S., Yang, J., 2022. FY4QPE-MSA: an All-Day Near-Real-Time Quantitative Precipitation Estimation Framework based on Multispectral Analysis from AGRI Onboard Chinese FY-4 Series Satellites. *IEEE Trans. Geosci. Remote Sens.* 60, 1–15. <https://doi.org/10.1109/TGRS.2022.3159036>.
- Michaelides, S., et al., 2009. Precipitation: Measurement, remote sensing, climatology and modeling. *Atmos. Res.* 94 (4), 512–533. <https://doi.org/10.1016/j.atmosres.2009.08.017>.
- Min, M., et al., 2019. Estimating Summertime Precipitation from Himawari-8 and Global Forecast System based on Machine Learning. *IEEE Trans. Geosci. Remote Sens.* 57 (5), 2557–2570. <https://doi.org/10.1109/TGRS.2018.2874950>.
- Min, M., Li, J., Wang, F., Liu, Z., Menzel, W.P., 2020. Retrieval of cloud top properties from advanced geostationary satellite imager measurements based on machine learning algorithms. *Remote Sens. Environ.* 239, 111616. <https://doi.org/10.1016/j.rse.2019.111616>.
- Minnis, P., et al., 2011. CERES Edition-2 Cloud Property Retrievals using TRMM VIRS and Terra and Aqua MODIS Data—Part I: Algorithms. *IEEE Trans. Geosci. Remote Sens.* 49, 4374–4400. <https://doi.org/10.1109/TGRS.2011.2144601>.
- Moazami, S., Najafi, M.R., 2021. A comprehensive evaluation of GPM-IMERG V06 and MRMS with hourly ground-based precipitation observations across Canada. *J. Hydrol.* 594, 125929. <https://doi.org/10.1016/j.jhydrol.2020.125929>.
- Morrison, H., et al., 2020. Confronting the Challenge of Modeling Cloud and Precipitation Microphysics. *J. Adv. Model. Earth Syst.* 12 (8), e2019MS001689. <https://doi.org/10.1029/2019MS001689>.
- Muñoz-Sabater, J., et al., 2021. ERA5-Land: a state-of-the-art global reanalysis dataset for land applications. *Earth Syst. Sci. Data* 13, 4349–4383. <https://doi.org/10.5194/essd-13-4349-2021>.
- Nakajima, T.Y., Suzuki, K., Stephens, G.L., 2010. Droplet Growth in warm Water Clouds Observed by the A-Train. Part II: a Multisensor View. *J. Atmos. Sci.* 67 (6), 1897–1907. <https://doi.org/10.1175/2010JAS3276.1>.
- Nascimento, J.G., et al., 2021. Evaluating the latest IMERG Products in a Subtropical climate: the Case of Paraná State, Brazil. *Remote Sens.* 13, 906. <https://doi.org/10.3390/rs13050906>.
- Nauss, T., Kokhanovsky, A.A., 2006. Discriminating raining from non-raining clouds at mid-latitudes using multispectral satellite data. *Atmos. Chem. Phys.* 6 (12), 5031–5036. <https://doi.org/10.5194/acp-6-5031-2006>.
- Nielsen, U.N., Ball, B.A., 2015. Impacts of altered precipitation regimes on soil communities and biogeochemistry in arid and semi-arid ecosystems. *Glob. Chang. Biol.* 21 (4), 1407–1421. <https://doi.org/10.1111/gcb.12789>.
- Okamoto, K.I., Ushio, T., Iguchi, T., Takahashi, N., Iwanami, K., 2005. The global satellite mapping of precipitation (GSMaP) project, Proceedings. In: 2005 IEEE International Geoscience and Remote Sensing Symposium, 2005. IGARSS '05, pp. 3414–3416. <https://doi.org/10.1109/IGARSS.2005.1526575>.
- Peinó, E., Bech, J., Udina, M., 2022. Performance Assessment of GPM IMERG Products at Different Time Resolutions, Climatic areas and Topographic Conditions in Catalonia. *Remote Sens.* 14, 5085. <https://doi.org/10.3390/rs14205085>.
- Peinó, E., Bech, J., Udina, M., Polls, F., 2024. Disentangling Satellite Precipitation Estimate Errors of Heavy Rainfall at the Daily and Sub-Daily Scales in the Western Mediterranean. *Remote Sens.* 16, 457. <https://doi.org/10.3390/rs16030457>.
- Peng, X., Li, Q., Jing, J., 2022. CNGAT: a Graph Neural Network Model for Radar Quantitative Precipitation Estimation. *IEEE Trans. Geosci. Remote Sens.* 60, 1–14. <https://doi.org/10.1109/TGRS.2021.3120218>.
- Peng, K., et al., 2023. Machine learning model to accurately estimate the planetary boundary layer height of Beijing urban area with ERA5 data. *Atmos. Res.* 293, 106925. <https://doi.org/10.1016/j.atmosres.2023.106925>.
- Platnick, S., 2000. Vertical photon transport in cloud remote sensing problems. *J. Geophys. Res. Atmos.* 105 (D18), 22919–22935. <https://doi.org/10.1029/2000JD900333>.
- Pradhan, R.K., et al., 2022. Review of GPM IMERG performance: a global perspective. *Remote Sens. Environ.* 268, 112754. <https://doi.org/10.1016/j.rse.2021.112754>.

- Prakash, S., Mitra, A.K., Pai, D.S., AghaKouchak, A., 2016. From TRMM to GPM: how well can heavy rainfall be detected from space? *Adv. Water Resour.* 88, 1–7. <https://doi.org/10.1016/j.advwatres.2015.11.008>.
- Prakash, S., et al., 2018. A preliminary assessment of GPM-based multi-satellite precipitation estimates over a monsoon dominated region. *J. Hydrol.* 556, 865–876. <https://doi.org/10.1016/j.jhydrol.2016.01.029>.
- Rafati, S., Khazaei, Z., Bahramnejad, S., 2024. Investigation of thermodynamics and dynamic factors affecting the development, strength, and longevity of mesoscale convective systems. *Theor. Appl. Climatol.* 155 (5), 3719–3737. <https://doi.org/10.1007/s00704-024-04844-7>.
- Ramadhan, R., et al., 2022. Evaluation of GPM IMERG Performance using Gauge Data over Indonesian Maritime Continent at Different Time Scales. *Remote Sens.* 14, 1172. <https://doi.org/10.3390/rs14051172>.
- Retalis, A., Katsanos, D., Tymvios, F., Michaelides, S., 2020. Comparison of GPM IMERG and TRMM 3B43 Products over Cyprus. *Remote Sens.* 12, 3212. <https://doi.org/10.3390/rs12193212>.
- Salamalikis, V., Argiriou, A.A., Dotsika, E., 2016. Isotopic modeling of the sub-cloud evaporation effect in precipitation. *Sci. Total Environ.* 544, 1059–1072. <https://doi.org/10.1016/j.scitotenv.2015.11.072>.
- Schmets, J., Tjemkes, S.A., Gube, M., van de Berg, L., 1997. Monitoring deep convection and convective overshooting with METEOSAT. *Adv. Space Res.* 19 (3), 433–441. [https://doi.org/10.1016/S0273-1177\(97\)00051-3](https://doi.org/10.1016/S0273-1177(97)00051-3).
- Shang, H., et al., 2024a. A hybrid cloud detection and cloud phase classification algorithm using classic threshold-based tests and extra randomized tree model. *Remote Sens. Environ.* 302, 113957. <https://doi.org/10.1016/j.rse.2023.113957>.
- Shang, N., et al., 2024b. Toward an Operational Machine-Learning-based Model for Deriving the Real-Time Gapless Diurnal Cycle of ozone Pollution in China with CLDAS Data. *Environ. Sci. Technol. Lett.* 11 (6), 553–559. <https://doi.org/10.1021/acs.estlett.4c00106>.
- Shen, Y., Xiong, A., 2015. Validation and comparison of a new gauge-based precipitation analysis over mainland China. *Int. J. Climatol.* 36. <https://doi.org/10.1002/joc.4341>.
- Skofronick-Jackson, G., et al., 2017. The Global Precipitation Measurement (GPM) Mission for Science and Society. *Bull. Am. Meteorol. Soc.* 98 (8), 1679–1695. <https://doi.org/10.1175/BAMS-D-15-00306.1>.
- Stephens, G.L., et al., 2012. An update on Earth's energy balance in light of the latest global observations. *Nat. Geosci.* 5 (10), 691–696. <https://doi.org/10.1038/ngeo1580>.
- Sun, L.X., Zhuge, X.Y., Wang, Y., 2019. A Contour-based Algorithm for Automated Detection of Overshooting Tops using Satellite infrared Imagery. *IEEE Trans. Geosci. Remote Sens.* 57 (1), 497–508. <https://doi.org/10.1109/TGRS.2018.2857486>.
- Tan, S., Chen, H., 2023. A Conditional Generative Adversarial Network for Weather Radar Beam Blockage Correction. *IEEE Trans. Geosci. Remote Sens.* 61, 1–14. <https://doi.org/10.1109/TGRS.2023.3286181>.
- Tang, G., Ma, Y., Long, D., Zhong, L., Hong, Y., 2016. Evaluation of GPM Day-1 IMERG and TMPA Version-7 legacy products over mainland China at multiple spatiotemporal scales. *J. Hydrol.* 533, 152–167. <https://doi.org/10.1016/j.jhydrol.2015.12.008>.
- Tang, G., Clark, M.P., Papalexiou, S.M., Ma, Z., Hong, Y., 2020. Have satellite precipitation products improved over last two decades? A comprehensive comparison of GPM IMERG with nine satellite and reanalysis datasets. *Remote Sens. Environ.* 240, 111697. <https://doi.org/10.1016/j.rse.2020.111697>.
- Teng, S., et al., 2020. Retrieval of Ice-Over-Water Cloud Microphysical and Optical Properties using Passive Radiometers. *Geophys. Res. Lett.* 47 (16), e2020GL088941. <https://doi.org/10.1029/2020GL088941>.
- Teng, S., et al., 2023. A multispectral method for retrieving overlapping cloud top heights from passive radiometers. *Remote Sens. Environ.* 286, 113425. <https://doi.org/10.1016/j.rse.2022.113425>.
- Thies, B., Nauss, T., Bendix, J., 2008a. Discriminating raining from non-raining cloud areas at mid-latitudes using meteosat second generation SEVIRI night-time data. *Meteorol. Appl.* 15 (2), 219–230. <https://doi.org/10.1002/met.56>.
- Thies, B., Nauss, T., Bendix, J., 2008b. Discriminating raining from non-raining clouds at mid-latitudes using meteosat second generation daytime data. *Atmos. Chem. Phys.* 8 (9), 2341–2349. <https://doi.org/10.5194/acp-8-2341-2008>.
- Tian, Y., et al., 2009. Component analysis of errors in satellite-based precipitation estimates. *J. Geophys. Res. Atmos.* 114 (D24). <https://doi.org/10.1029/2009JD011949>.
- Wang, Z., Zhong, R., Lai, C., Chen, J., 2017. Evaluation of the GPM IMERG satellite-based precipitation products and the hydrological utility. *Atmos. Res.* 196, 151–163. <https://doi.org/10.1016/j.atmosres.2017.06.020>.
- Wang, C., Xu, J., Tang, G., Yang, Y., Hong, Y., 2020. Infrared Precipitation Estimation using Convolutional Neural Network. *IEEE Trans. Geosci. Remote Sens.* 58 (12), 8612–8625. <https://doi.org/10.1109/TGRS.2020.2989183>.
- Wang, Q., et al., 2022a. Retrieval of cloud properties from thermal infrared radiometry using convolutional neural network. *Remote Sens. Environ.* 278, 113079. <https://doi.org/10.1016/j.rse.2022.113079>.
- Wang, X., Iwabuchi, H., Yamashita, T., 2022b. Cloud identification and property retrieval from Himawari-8 infrared measurements via a deep neural network. *Remote Sens. Environ.* 275, 113026. <https://doi.org/10.1016/j.rse.2022.113026>.
- Wei, J., et al., 2021. Himawari-8-derived diurnal variations in ground-level PM_{2.5} pollution across China using the fast space-time Light Gradient Boosting Machine (LightGBM). *Atmos. Chem. Phys.* 21 (10), 7863–7880. <https://doi.org/10.5194/acp-21-7863-2021>.
- Wu, J., et al., 2024. Can ERA5 reanalysis data characterize the pre-storm environment? *Atmos. Res.* 297, 107108. <https://doi.org/10.1016/j.atmosres.2023.107108>.
- Xie, P., et al., 2017. Reprocessed, Bias-Corrected CMORPH Global High-Resolution Precipitation estimates from 1998. *J. Hydrometeorol.* 18, 1617–1641. <https://doi.org/10.1175/JHM-D-16-0168.1>.
- Yan, Y., Liu, Y., 2019. Vertical Structures of Convective and Stratiform Clouds in Boreal Summer over the Tibetan Plateau and its Neighboring Regions. *Adv. Atmos. Sci.* 36 (10), 1089–1102. <https://doi.org/10.1007/s00376-019-8229-4>.
- Yang, B., et al., 2018. Simulated precipitation diurnal cycles over East Asia using different CAPE-based convective closure schemes in WRF model. *Clim. Dyn.* 50 (5), 1639–1658. <https://doi.org/10.1007/s00382-017-3712-z>.
- Yang, Y., et al., 2022. Machine learning-based retrieval of day and night cloud macrophysical parameters over East Asia using Himawari-8 data. *Remote Sens. Environ.* 273, 112971. <https://doi.org/10.1016/j.rse.2022.112971>.
- Yang, W., Chen, H., Han, L., Ge, Y., 2023. Multitask Learning for Precipitation Estimation using Satellite Observations from the GOES-R Series. *IEEE Geosci. Remote Sens. Lett.* 20, 1–5. <https://doi.org/10.1109/LGRS.2023.3313150>.
- Ye, B.-Y., Lee, G., Park, H.-M., 2015. Identification and removal of non-meteorological echoes in dual-polarization radar data based on a fuzzy logic algorithm. *Adv. Atmos. Sci.* 32 (9), 1217–1230. <https://doi.org/10.1007/s00376-015-4092-0>.
- You, Y., Liu, G., 2012. The relationship between surface rainrate and water paths and its implications to satellite rainrate retrieval. *J. Geophys. Res. Atmos.* 117 (D13). <https://doi.org/10.1029/2012JD017662>.
- Yu, R., Li, J., Chen, H., Yuan, W., 2014. Progress in studies of the precipitation diurnal variation over contiguous China. *J. Meteorol.* 28 (5), 877–902. <https://doi.org/10.1007/s13351-014-3272-7>.
- Zhao, Y., Li, J., Zhang, W., Deng, C., Li, Y., 2022. Cloud Response is significantly Biased by CMIP6 over the Tibetan Plateau. *Geophys. Res. Lett.* 49 (17), e2022GL100903. <https://doi.org/10.1029/2022GL100903>.
- Zhang, Z., Johansson, C., Engardt, M., Stafoggia, M., Ma, X., 2024. Improving 3-day deterministic air pollution forecasts using machine learning algorithms. *Atmos. Chem. Phys.* 24, 807–851. <https://doi.org/10.5194/acp-24-807-2024>.
- Zhao, Y., et al., 2023. Diurnal cycles of cloud cover and its vertical distribution over the Tibetan Plateau revealed by satellite observations, reanalysis datasets, and CMIP6 outputs. *Atmos. Chem. Phys.* 23 (1), 743–769. <https://doi.org/10.5194/acp-23-743-2023>.
- Zhao, C., et al., 2024a. Observational evidence and mechanisms of aerosol effects on precipitation. *Sci. Bull.* 69 (10), 1569–1580. <https://doi.org/10.1016/j.scib.2024.03.014>.
- Zhao, Y., Li, J., Wang, Y., Zhang, W., Wen, D., 2024b. Warming Climate-Induced changes in Cloud Vertical distribution possibly Exacerbate Intra-Atmospheric heating over the Tibetan Plateau. *Geophys. Res. Lett.* 51 (3), e2023GL107713. <https://doi.org/10.1029/2023GL107713>.
- Zheng, Y., Gong, Y., Chen, J., Tian, F., 2019. Warm-season Diurnal Variations of Total, Stratiform, Convective, and Extreme Hourly Precipitation over Central and Eastern China. *Adv. Atmos. Sci.* 36 (2), 143–159. <https://doi.org/10.1007/s00376-018-7307-3>.
- Zhou, K., Sun, J., Zheng, Y., Zhang, Y., 2022. Quantitative Precipitation Forecast Experiment based on Basic NWP Variables using Deep Learning. *Adv. Atmos. Sci.* 39 (9), 1472–1486. <https://doi.org/10.1007/s00376-021-1207-7>.
- Zhu, S., Ma, Z., 2022. PECA-FY4A: Precipitation Estimation using Chromatographic Analysis methodology for full-disc multispectral observations from FengYun-4A/AGRI. *Remote Sens. Environ.* 282, 113234. <https://doi.org/10.1016/j.rse.2022.113234>.
- Zhugue, X., et al., 2024. Introduction to the NJIAS Himawari-8/9 Cloud Feature Dataset for climate and typhoon research. *Earth Syst. Sci. Data* 16 (4), 1747–1769. <https://doi.org/10.5194/essd-16-1747-2024>.